The Astrophysical Journal, 744:154 (17pp), 2012 January 10 doi:10.1088/0004-637X/744/2/154

GOODS-*HERSCHEL* MEASUREMENTS OF THE DUST ATTENUATION OF TYPICAL STAR-FORMING GALAXIES AT HIGH REDSHIFT: OBSERVATIONS OF ULTRAVIOLET-SELECTED GALAXIES AT $z \sim 2$*

N. Reddy[1,2,19], M. Dickinson[1], D. Elbaz[3], G. Morrison[4,5], M. Giavalisco[6], R. Ivison[7,8], C. Papovich[9], D. Scott[10], V. Buat[11], D. Burgarella[11], V. Charmandaris[12,13,14], E. Daddi[3], G. Magdis[3], E. Murphy[15], B. Altieri[16], H. Aussel[3], H. Dannerbauer[3], K. Dasyra[3], H. S. Hwang[3], J. Kartaltepe[1], R. Leiton[3,17], B. Magnelli[3], and P. Popesso[18]

[1] National Optical Astronomy Observatory, 950 N Cherry Ave, Tucson, AZ 85719, USA
[2] Department of Physics and Astronomy, University of California, Riverside, 900 University Avenue, Riverside, CA 92521, USA
[3] Laboratoire AIM-Paris-Saclay, CEA/DSM/Irfu-CNRS-Université Paris Diderot, CE-Saclay, F-91191, Gif-sur-Yvette, France
[4] Institute for Astronomy, University of Hawaii, Honolulu, HI 96822, USA
[5] Canada–France–Hawaii Telescope, Kamuela, HI 96743, USA
[6] Astronomy Department, University of Massachusetts, Amherst, Amherst, MA 01003, USA
[7] UK Astronomy Technology Centre, Science and Technology Facilities Council, Royal Observatory, Blackford Hill, Edinburgh EH9 3HJ, UK
[8] Institute for Astronomy, University of Edinburgh, Blackford Hill, Edinburgh EH9 3HJ, UK
[9] Department of Physics and Astronomy, Texas A&M University, College Station, TX 77845, USA
[10] Department of Physics and Astronomy, University of British Columbia, Vancouver, BC V6T 1Z1, Canada
[11] Laboratoire d'Astrophysique de Marseille, OAMP, Université Aix-Marseille, CNRS, 38 Rue Frédéric Joliot-Curie, 13388 Marseille Cedex 13, France
[12] Department of Physics and Institute of Theoretical & Computational Physics, University of Crete, GR-71003, Heraklion, Greece
[13] IESL/Foundation for Research & Technology-Hellas, GR-71110, Heraklion, Greece
[14] Chercheur Associé, Observatoire de Paris, F-75014 Paris, France
[15] *Spitzer* Science Center, MC 314-6, California Institute of Technology, Pasadena, CA 91125, USA
[16] *Herschel* Science Centre, European Space Astronomy Centre, Villanueva de la Cañada, 28691 Madrid, Spain
[17] Astronomy Department, Universidad de Concepción, Concepción, Chile
[18] Max-Planck-Institut für Extraterrestrische Physik (MPE), Postfach 1312, 85741 Garching, Germany
Received 2011 July 8; accepted 2011 October 26; published 2011 December 22

ABSTRACT

We take advantage of the sensitivity and resolution of the *Herschel Space Observatory* at 100 and 160 μm to directly image the thermal dust emission and investigate the infrared luminosities ($L_{\rm IR}$) and dust obscuration of typical star-forming (L^*) galaxies at high redshift. Our sample consists of 146 UV-selected galaxies with spectroscopic redshifts $1.5 \leqslant z_{\rm spec} < 2.6$ in the GOODS-North field. Supplemented with deep Very Large Array and *Spitzer* imaging, we construct median stacks at the positions of these galaxies at 24, 100, and 160 μm, and 1.4 GHz. The comparison between these stacked fluxes and a variety of dust templates and calibrations implies that typical star-forming galaxies with UV luminosities $L_{\rm UV} \gtrsim 10^{10}\ L_\odot$ at $z \sim 2$ are luminous infrared galaxies with a median $L_{\rm IR} = (2.2 \pm 0.3) \times 10^{11}\ L_\odot$. Their median ratio of $L_{\rm IR}$ to rest-frame 8 μm luminosity (L_8) is $L_{\rm IR}/L_8 = 8.9 \pm 1.3$ and is ≈80% larger than that found for most star-forming galaxies at $z \lesssim 2$. This apparent redshift evolution in the $L_{\rm IR}/L_8$ ratio may be tied to the trend of larger infrared luminosity surface density for $z \gtrsim 2$ galaxies relative to those at lower redshift. Typical galaxies at $1.5 \leqslant z < 2.6$ have a median dust obscuration $L_{\rm IR}/L_{\rm UV} = 7.1 \pm 1.1$, which corresponds to a dust correction factor, required to recover the bolometric star formation rate (SFR) from the unobscured UV SFR, of 5.2 ± 0.6. This result is similar to that inferred from previous investigations of the UV, Hα, 24 μm, radio, and X-ray properties of the same galaxies studied here. Stacking in bins of UV slope (β) implies that L^* galaxies with redder spectral slopes are also dustier and that the correlation between β and dustiness is similar to that found for local starburst galaxies. Hence, the rest-frame ≃30 and 50 μm fluxes validate on average the use of the local UV attenuation curve to recover the dust attenuation of typical star-forming galaxies at high redshift. In the simplest interpretation, the agreement between the local and high-redshift UV attenuation curves suggests a similarity in the dust production and stellar and dust geometries of starburst galaxies over the last 10 billion years.

Key words: dust, extinction – galaxies: high-redshift – infrared: galaxies

Online-only material: color figures

1. INTRODUCTION

A key aspect of measuring total star formation rates (SFRs) is to assess how a galaxy's spectral energy distribution (SED) is modulated by the effects of interstellar dust. The ability to quantify dust attenuation at high redshift is hindered by the limited dynamic range in luminosity at wavelengths that are sensitive to dust emission. While the Lyman Break technique (Steidel et al. 1995) has proven to be the most effective method of identifying galaxies across a large dynamic range in luminosity and lookback time, it requires observations in the rest-frame UV: the massive stars giving rise to the UV continuum also produce much of the dust that attenuates this continuum. The diminution of UV light is compounded by the fact that much of this radiation is re-emitted in the far-infrared where current instrumental sensitivity is insufficient to directly detect typical star-forming galaxies at $z \gtrsim 2$. It has therefore become common to use local relations between monochromatic and bolometric luminosity to infer the SFRs and dust attenuation of high-redshift galaxies.

* *Herschel* is an ESA space observatory with science instruments provided by European-led Principal Investigator consortia and with important participation from NASA.
[19] Hubble Fellow.

Prior to the era of large-scale multi-wavelength surveys like GOODS (Dickinson et al. 2003; Giavalisco et al. 2004), inferring the dust attenuation at high redshift commonly entailed using relations between the variation of the UV continuum slope with dustiness as found for local starburst galaxies (Meurer et al. 1999; Calzetti et al. 2000; Heckman et al. 1998). However, such correlations were previously untested at high redshift. The correlation between the redness of the UV slope (β) and dust attenuation has limited applicability when examined over a larger range in galaxy stellar population and luminosity. Galaxies with older and less massive stars contributing significantly to the UV emission can also exhibit a redder spectral slope (Calzetti 1997; Kong et al. 2004; Buat et al. 2005). Further, the UV slope decouples from extinction for very luminous galaxies where virtually all of the star formation is obscured, such as is the case for low-redshift ultra-luminous infrared galaxies (ULIRGs; Goldader et al. 2002). Nonetheless, the local trend between UV slope and dustiness is still applied widely to galaxies at high redshift; this correlation is often the only means by which one can infer the dust attenuation of galaxies at $z \gtrsim 3$, where the dust emission from a typical galaxy may be several orders of magnitude below the sensitivity limits of current infrared instruments.

Incremental progress in determining dust attenuation at high redshift was achieved with the first ultra-deep radio and X-ray surveys (e.g., Richards 2000; Alexander et al. 2003). Though the sensitivity (even at GOODS-depth) at these wavelengths was insufficient to individually detect typical star-forming galaxies at $z \gtrsim 2$, these surveys did allow for estimates of the mean dust attenuation based on stacking analyses. Initial studies suggested a general agreement between UV and radio/X-ray inferences of dust attenuation at $z \sim 2$–3 (Nandra et al. 2002; Seibert et al. 2002; Reddy & Steidel 2004; Reddy et al. 2005, 2006b; Daddi et al. 2007; Pannella et al. 2009).

The launch of the *Spitzer Space Telescope* enabled the first direct detection of the dust emission in non-lensed L^* galaxies at $z \sim 2$; at these redshifts, *Spitzer*'s MIPS (Multiband Imaging Photometer for *Spitzer*) 24 μm band is sensitive to the strongest dust emission feature (at 7.7 μm) in star-forming galaxies. This feature arises from the stochastic UV photoheating of small dust grains and hydrocarbons (e.g., Puget & Leger 1989; Tielens et al. 1999) and is found to correlate with the UV radiation from OB stars (e.g., Förster Schreiber et al. 2004; Roussel et al. 2001), albeit with significant scatter (e.g., Kennicutt et al. 2009; Hogg et al. 2005; Helou et al. 2001; Engelbracht et al. 2005; Normand et al. 1995). Several studies have demonstrated that the dust attenuation inferred from the UV spectral slope, β, for typical $z \sim 2$ galaxies is in general agreement with that inferred from MIPS 24 μm (e.g., Reddy et al. 2006b, 2010; Daddi et al. 2007). Regardless, local studies of resolved galaxies have emphasized the complexity of the 8 μm emission and the need to combine it with other obscured (IR) and unobscured (UV, Hα) tracers of star formation in order to obtain the most reliable measure of the bolometric luminosity (Kennicutt et al. 2009).

To this end, we take advantage of the improved sensitivity of *Herschel*/PACS (Photodetector Array Camera and Spectrometer) at 100 and 160 μm (Pilbratt et al. 2010; Poglitsch et al. 2010) to measure directly for the first time the thermal dust emission from a large sample of typical (L^*) star-forming galaxies at $z \sim 2$. We make use of the deep PACS data made possible by the GOODS-*Herschel* Open Time Key project (PI: D. Elbaz). We supplement these data with deep Very Large Array (VLA) 1.4 GHz continuum imaging in the GOODS-North field (Morrison et al. 2010). The primary aim is to constrain the average infrared luminosities of galaxies at high redshift, particularly those selected by their rest-frame UV colors, and to compare them to UV-based inferences. We begin in Section 2 by discussing the UV-selected galaxies and previous efforts to measure their stellar populations and dust attenuation. We also provide a brief description of the *Herschel* and radio data. Our stacking method and stacking simulations are described in Section 3, followed by a discussion of the dust SED fits to the stacked fluxes and the total infrared luminosities in Section 4. In Section 5, we proceed to compare the *Herschel*-based inferences of the dust attenuation with that inferred from the UV slope and discuss systematics in the dust obscuration with stellar population age and bolometric and UV luminosity. For ease of comparison with other studies, we assume a Salpeter (1955) initial mass function (IMF) and adopt a cosmology with $H_0 = 70$ km s^{-1} Mpc^{-1}, $\Omega_\Lambda = 0.7$, and $\Omega_m = 0.3$.

2. SAMPLE SELECTION AND *HERSCHEL*/PACS 100 AND 160 μm DATA

2.1. Rest-frame UV-selected Sample of Star-forming Galaxies at $z \sim 2$–3

The GOODS-North field was targeted as part of an ongoing imaging and spectroscopic survey of UV-selected galaxies at $z \sim 2$–3 (Steidel et al. 2004), primarily to take advantage of the extensive multi-wavelength data that exist for this field. Spectroscopic catalogs and analysis of the GOODS-North sample, including the stellar masses and dust attenuation of L^* galaxies at $z \sim 2$–3, are presented in Reddy et al. (2006a). Briefly, the galaxies were selected to lie at redshifts $1.5 \lesssim z \lesssim 3.4$ based on the "BM," "BX," and Lyman break galaxy (LBG) color criteria (Steidel et al. 2003, 2004; Adelberger et al. 2004). Extensive spectroscopic followup of candidates brighter than $\mathcal{R} = 25.5$ was conducted using the blue arm of the Low Resolution Imaging Spectrograph (LRIS; Steidel et al. 2004) on the Keck I telescope.

The criteria used to construct our sample are identical to those of Reddy et al. (2010). Only galaxies with secure spectroscopic redshifts $1.5 \leqslant z_{\rm spec} \leqslant 2.6$ were considered as this is the redshift range over which the MIPS band is sensitive to rest-frame 8 μm emission. Galaxies with any active galactic nucleus signatures based on optical emission lines (Lyα, C IV, N V) or a power-law SED through the Infrared Array Camera (IRAC) and MIPS 24 μm bands were excluded. Additionally, galaxies were included only if we were able to obtain robust point-spread function (PSF) fits to their 24 μm emission; in practice, this meant that a few galaxies were rejected because they are confused with nearby neighbors (see Reddy et al. 2010 for the parameter used to measure the degeneracy of the PSF fits). This sample forms the basis of our stacking analysis and includes a total of 146 galaxies, approximately 30% of which are detected with greater than 3σ significance in the GOODS-N 24 μm data.

2.2. Properties of the Sample and SED Modeling

Reddy & Steidel (2009) use a larger spectroscopic and photometric sample (the latter extending to $\mathcal{R} \sim 27.0$) in 31 independent fields to quantify the selection function for the UV sample and determine the UV luminosity function (LF) at $z \sim 2$. This analysis indicates that UV-selected galaxies commonly targeted for spectroscopy with $\mathcal{R} \lesssim 25.5$ have luminosities similar to L^* of the UV LF, where $L^*_{\rm UV} \approx 4 \times 10^{10}\ L_\odot$ (Reddy & Steidel 2009). Throughout the text, L^* refers to the characteristic

luminosity of the UV LF, unless stated otherwise. The stellar populations of these galaxies have been modeled previously, and we refer the reader to Reddy et al. (2010) for a detailed description of the modeling procedure.

Briefly, S. Charlot & G. Bruzual (2011, in preparation) stellar population models with a range of exponentially declining star formation histories τ = 10, 20, 50, 100, 200, 500, 1000, 2000, and 5000 Myr, as well as a constant star formation (CSF) history, were fit to the observed $U_nG\mathcal{R}$, JK_s, and *Spitzer*/IRAC data. In addition, we considered ages spaced roughly logarithmically between 70 and 5000 Myr, excluding any that are older than the age of the universe at the redshift of each galaxy. The lower limit to the allowed ages (70 Myr) was adopted to reflect the typical dynamical timescale as inferred from velocity dispersion and size measurements of $z \sim 2$ LBGs (Erb et al. 2006; Law et al. 2007). Reddening was incorporated by employing the Calzetti et al. (2000) attenuation curve and allowing $E(B-V)$ to range between 0.0 and 0.6.

We adopt the best-fit stellar population parameters obtained when assuming a CSF history, unless an exponentially declining (τ) model gives a significantly better fit to the broadband data. Generally, the χ^2 values assuming the CSF model were similar to those obtained when τ is allowed to vary freely. Further, more extreme star formation histories, where the ratio of the age to τ is much greater than unity, i.e., $t_{\rm age}/\tau \gg 1$, can be ruled out based on the presence of O star and Wolf-Rayet features in the composite UV spectra of $z \sim 2$ galaxies, as well as the fact that such models often predict ages that are unrealistically much younger than the dynamical timescale at $z \sim 2$. For the present analysis, we use the results of the stellar population modeling to distinguish those galaxies that have young star formation ages $\lesssim$100 Myr. Such galaxies have been shown previously to depart from the UV attenuation curve established for more typical galaxies at $z \sim 2$ (Reddy et al. 2006b, 2010), and we wish to explore this difference with the *Herschel* data.

2.3. Construction of Subsamples

The sample of 146 UV-selected galaxies was subdivided into subsamples in order to investigate the differences in dust attenuation between galaxies with blue and red UV spectral slopes, those with high bolometric luminosities ($L_{\rm bol} \equiv L_{\rm IR} + L_{\rm UV}$), and those with young stellar population ages. The properties of these subsamples, including the criteria used to construct them, the number of galaxies in each subsample, and their β and redshift distributions, are summarized in Table 1. As noted above, the ages are estimated from stellar population modeling of the rest-frame UV through *Spitzer* IRAC photometry. For the purpose of constructing the subsamples, we estimated bolometric luminosities based on the Reddy et al. (2010) calibration between 8 μm and infrared luminosity (see the next section). Finally, UV slopes β were determined from the $G-\mathcal{R}$ colors of galaxies as follows. We generated power laws in $f(\lambda) \propto \lambda^{\beta}$ for $-2.5 \leqslant \beta \leqslant 1.0$ with $\Delta\beta = 0.01$. These were attenuated for the Lyα forest opacity assuming the Madau (1995) prescription and multiplied by the G and $\mathcal{R}$ transmission filters. The G band is affected by the Lyα forest only for redshifts $z \gtrsim 2.5$; statistical fluctuations in the forest will not affect β as most of the galaxies considered here lie at redshifts $z \leqslant 2.5$. For this same reason, Lyα lies outside of the G-band filter and will therefore not affect β. The UV slope for a given galaxy is taken to be the one which gives the closest match in $G-\mathcal{R}$ color to the observed value. The error in UV slope is related directly to the error in color and is typically $\sigma_\beta \simeq 0.11$.

2.4. Previous MIPS Results

To provide a context for our present analysis, we briefly summarize previous efforts to constrain the dust emission and bolometric luminosities of galaxies at $z \sim$ 2–3. Reddy et al. (2006b) investigated the variation in 24 μm flux with dust-corrected UV and X-ray measures of the bolometric luminosities of the same UV-selected galaxies analyzed here. Extending upon this result, Reddy et al. (2010) used a sample of 90 LBGs to examine the relationship between rest-frame 8 μm ($\nu L_\nu[8\,\mu{\rm m}] \equiv L_8$) and H$\alpha$ luminosity at $z \sim 2$, finding a tight trend between the two, with a scatter of $\approx$0.24 dex. Using Hα luminosity as a proxy for total SFR—after accounting for dust with a Calzetti et al. (2000) attenuation curve—then allowed these authors to establish a relationship between L_8 and dust obscured SFR, or $L_{\rm IR}$.

The previous studies found that typical (L^*) star-forming galaxies at $z \sim 2$ have dust attenuations, or infrared-to-UV luminosity ratios, $L_{\rm IR}/L_{\rm UV} \simeq 5$, similar to the values predicted from the UV slope, β, using the local correlation between β and $L_{\rm IR}/L_{\rm UV}$ (Meurer et al. 1999). Investigations of the 24 μm emission of galaxies selected at rest-frame optical wavelengths—resulting in samples that are not orthogonal to the one analyzed here—have reached similar conclusions regarding the validity of UV-based dust corrections for moderately luminous galaxies at $z \sim 2$ (Daddi et al. 2007). These results have been extended to higher redshift: Magdis et al. (2010a) demonstrate that UV-based dust corrections for LBGs at $z \sim 3$ yield bolometric luminosities comparable to those inferred from infrared, radio, and millimeter measures. The 160 μm emission from $z \sim 3$ LBGs also corresponds to $L_{\rm IR}$ that are similar to those obtained with 24 μm estimates (Magdis et al. 2010b). While this is important validation of our understanding of star formation and dust obscuration at high redshift, the LBGs that Magdis et al. (2010b) detected in stacked 160 μm data have significantly higher luminosities ($\langle L_{\rm IR}\rangle \approx 1.6 \times 10^{12}\,L_\odot$) and SFRs ($>100\,M_\odot\ {\rm yr}^{-1}$) than those of the typical L^* galaxies analyzed here.

In any case, while this agreement is encouraging, and instills confidence in our ability to recover the dust attenuation of typical galaxies from measurements of their UV continuum slopes, uncertainties in the k-corrections and the conversion between 8 μm and infrared luminosity (as well as conversion between X-ray emission and SFR, for the X-ray stacking analyses) no doubt introduce some scatter in the inferred dust obscurations. The primary goal of our present analysis is to obtain more direct measures of the total infrared luminosities of $z \sim 2$ galaxies using *Herschel* data, which are described below.

2.5. Herschel and VLA Data

The GOODS-*Herschel* Open Time Key Program (PI: D. Elbaz) includes $\approx$124 hr of 100 and 160 μm PACS imaging and 31 hr of Spectral and Photometric Imaging Receiver (SPIRE) imaging in the GOODS-North field. The 3σ depths of the PACS 100 and 160 μm images are 1.1 mJy and 2.6 mJy, respectively. None of the galaxies in the sample analyzed here are detected to these depths. Further details on the data reduction are given in Elbaz et al. (2011). PSFs were constructed based on the catalogs of *Herschel* detections discussed in Elbaz et al. (2011). When performing PSF photometry, we adjusted all fluxes upward by multiplicative factors of 1.37 and 1.29 at 100 and 160 μm, respectively, to account for missing flux in the wings of the PSFs. The similar factor for the MIPS 24 μm PSF is 1.22.

Table 1
Properties of the Stacks I: 100 μm Fluxes, Redshifts, and UV Slopes

Sample	Criterion[a]	f_{100} $r_{exc} = 3\farcs43$[b]	f_{100} No Exclusion[c]
A.	All	$(3.0 \pm 0.5) \times 10^{-4}$ Jy	$(3.0 \pm 0.4) \times 10^{-4}$ Jy
All		$N = 106$	$N = 146$
UV-selected		$\langle\beta\rangle = -1.41 \pm 0.42$	$\langle\beta\rangle = -1.41 \pm 0.41$
		$\langle z\rangle = 2.08 \pm 0.24$	$\langle z\rangle = 2.08 \pm 0.26$
B.	Age $\gtrsim$ 100 Myr;	$(2.4 \pm 0.5) \times 10^{-4}$ Jy	$(2.8 \pm 0.5) \times 10^{-4}$ Jy
L^* Galaxies	$L_{bol} \leqslant 10^{12}\ L_\odot$	$N = 83$	$N = 114$
		$\langle\beta\rangle = -1.48 \pm 0.37$	$\langle\beta\rangle = -1.46 \pm 0.38$
		$\langle z\rangle = 2.09 \pm 0.24$	$\langle z\rangle = 2.09 \pm 0.25$
C.	Age $\gtrsim$ 100 Myr;	$(1.9 \pm 0.7) \times 10^{-4}$ Jy	$(2.1 \pm 0.7) \times 10^{-4}$ Jy
Blue	$L_{bol} \leqslant 10^{12}\ L_\odot$;	$N = 51$	$N = 67$
UV slopes	$\beta < -1.4$	$\langle\beta\rangle = -1.61 \pm 0.21$	$\langle\beta\rangle = -1.59 \pm 0.21$
		$\langle z\rangle = 2.05 \pm 0.24$	$\langle z\rangle = 2.05 \pm 0.26$
D.	Age $\gtrsim$ 100 Myr;	$(3.8 \pm 0.9) \times 10^{-4}$ Jy	$(3.4 \pm 0.6) \times 10^{-4}$ Jy
Red	$L_{bol} \leqslant 10^{12}\ L_\odot$;	$N = 32$	$N = 47$
UV slopes	$\beta \geqslant -1.4$	$\langle\beta\rangle = -1.10 \pm 0.26$	$\langle\beta\rangle = -1.15 \pm 0.26$
		$\langle z\rangle = 2.19 \pm 0.22$	$\langle z\rangle = 2.14 \pm 0.24$
E.	Age $\gtrsim$ 100 Myr;	$(11.0 \pm 1.7) \times 10^{-4}$ Jy	$(9.9 \pm 1.2) \times 10^{-4}$ Jy
ULIRGs	$L_{bol} > 10^{12}\ L_\odot$	$N = 9$	$N = 12$
		$\langle\beta\rangle = -0.84 \pm 0.48$	$\langle\beta\rangle = -0.84 \pm 0.46$
		$\langle z\rangle = 2.03 \pm 0.27$	$\langle z\rangle = 2.22 \pm 0.29$
		$\langle L_{bol}\rangle = (1.3 \pm 0.1) \times 10^{12}\ L_\odot$	$\langle L_{bol}\rangle = (1.3 \pm 0.1) \times 10^{12}\ L_\odot$
		$L_{bol}^{max} = 1.8 \times 10^{12}\ L_\odot$	$L_{bol}^{max} = 1.8 \times 10^{12}\ L_\odot$
F.	Age $\lesssim$100 Myr	3σ: $< 4.4 \times 10^{-4}$ Jy	3σ: $< 3.2 \times 10^{-4}$ Jy
Young		$N = 14$	$N = 20$
Galaxies		$\langle\beta\rangle = -1.17 \pm 0.40$	$\langle\beta\rangle = -1.30 \pm 0.40$
		$\langle z\rangle = 2.00 \pm 0.26$	$\langle z\rangle = 2.00 \pm 0.28$

Notes. Each entry includes (a) the stacked flux at 100 μm and its measurement uncertainty; (b) the number of galaxies contributing to the stack; and (c) the mean and sample dispersion of the UV slopes (β) and redshifts of those galaxies. We assign 3σ upper limits to fluxes in cases where the 1σ measurement uncertainty is larger than the stacked flux. For Sample E (ULIRGs), we include the mean and error in the mean of the bolometric luminosity (L_{bol}; derived using the calibration of Reddy et al. 2010) and the maximum bolometric luminosity (L_{bol}^{max}) contributing to the stack.

[a] The criteria used to select each subsample are listed here. The ages were determined from SED fitting to the broadband photometry (see the text) and the bolometric luminosities, L_{bol}, were determined from our previous calibration between 24 μm and infrared luminosity (Reddy et al. 2010).

[b] Criteria for excluding galaxies from the stack. If any galaxy lies within a distance r_{exc} of a nearby optical, K_s-band, or IRAC source, it is excluded from the stack.

[c] No-exclusion radius adopted; all galaxies are median stacked.

The VLA radio 1.4 GHz data are described in Morrison et al. (2010). Briefly, a total of 165 hr of observations, including 42 hr from Richards (2000), were combined to produce a radio map of the GOODS-North field. The noise level of the image is $\sim$3.9 μJy beam^{-1} near the center and $\sim$8 μJy beam^{-1} at 15′ from the center. The synthesized beam size of the radio data is $\sim 1\farcs7 \times 1\farcs6$, corresponding to a physical scale of 14.1×13.3 kpc at $z = 2.30$. The radio map used in the stacking analysis is primary beam corrected.

3. STACKING METHOD AND SIMULATIONS

3.1. General Stacking Procedure

The method used to stack the *Herschel* 100 and 160 μm, *Spitzer* 24 μm, and the VLA radio data is as follows. We extracted an area $50'' \times 50''$ around each object to be stacked. The area was chosen to be large enough to obtain a reliable estimate of the local background. These cutouts were then median combined after rotating each sub-image by 90° relative the previous sub-image contributing to the stack, in order to minimize image defects that are aligned with the scanning orientation of the data acquisition.[20] We adopted the median stacks to ensure the results are not biased by bright outliers. We stacked the 24 μm data in exactly the same way as was done for the 100 and 160 μm data, irrespective of whether a galaxy was directly detected at 24 μm, in order to ensure the most consistent results across wavelengths.

To test the effects of a non-negligible amount of flux in the wings of the stacked signal relative to the PSF (due to positional uncertainty), we performed both PSF-fitting photometry and simple aperture photometry on the stacked flux. The background and measurement uncertainty in the stacked image are taken, respectively, to be the mean and 1σ dispersion in flux computed by fitting many PSFs at random positions in the stacked image. We simultaneously fit the target flux (with a PSF) and a constant value to account for the background level in the stacked image. We found no significant systematic bias in the aperture versus PSF-derived flux relative to the measurement uncertainties, and

[20] To test for any systematic effect associated with asymmetries in the PSF, we also stacked without rotating each sub-image. The results obtained with and without rotating the sub-images were identical within the uncertainties of the stacked flux measurements.

we adopted the PSF-determined flux measurements. For the radio data, the PSF-measured flux and total integrated flux differ by ≈20%–30% due to bandwidth smearing. To account for this effect, we have adopted the fluxes computed from fitting the best-fit elliptical Gaussian profile (with peak intensity normalized to unity) to the stacked radio emission, yielding the integrated flux density.

3.2. Residual Images

Residual maps at 100 and 160 μm were constructed in order to quantify any systematic effect on the stacked fluxes from nearby bright sources.[21] Sources detected at $>3\sigma$ were subtracted from the science mosaics (none of the galaxies in our sample are detected at 100 and 160 μm at this level). We considered detections based both on a blind catalog ("blind-subtracted"), where a detection algorithm was used directly on the PACS mosaics, as well as a catalog constructed using 24 μm priors to define the positions of sources in the longer wavelength PACS bands ("prior-subtracted"). In both cases, we used PSF photometry to determine the fluxes of sources and subtract them from the science images. To ensure that there are no systematic effects that may bias the flux measurement made on the residual maps, we performed the same stacking analysis on the science images themselves. Comparison between the stacks on the blind-residual maps, prior-residual maps, and the science images, showed that the stacked fluxes were within 10% of each other. Typically, the stacked fluxes measured on the science images were *lower* than those measured on the residual images. This effect is attributed to the higher background level in the stack derived from the science images due to the PSF wings of nearby sources. The similarity in flux regardless of the image used for the stack suggests that the median combination of sub-images is robust to bright outliers, as expected. The flux measurements obtained by stacking on the prior-fit residual maps are adopted for further analysis. The median stacked data for L^* galaxies (Sample B, Table 1) at 24, 100, and 160 μm, and 1.4 GHz are shown in Figure 1.

3.3. Exclusion Tests and Simulations

A common concern in stacking data with relatively poor resolution is the potential contribution from unrelated sources within the beam that are formally undetected (i.e., with a $<3\sigma$ significance) and which therefore remain in the residual images, but which may contribute significantly to the stacked flux. If these unrelated sources have a random spatial distribution, then their contribution to the stacked flux will be accounted for when we subtract the background in the stacked images. However, if the unrelated sources are clustered with respect to the UV-selected galaxies, they will contribute to the stacked fluxes. To test for the effect of clustering on the stacked fluxes, we considered a number of tests, as we describe below.

3.3.1. Exclusion Radius

The most conservative measure of the median flux can be achieved by stacking only those galaxies without any nearby sources. The full width at half-maximum (FWHM) of the PSF at 100 μm is small enough ($\simeq 6''$) such that we can adopt an "exclusion radius" $r_{\rm exc}$ = FWHM/2, and still have enough galaxies to stack. We first constructed a catalog containing

[21] We did not construct a residual map for the VLA data given the higher resolution of these data and the lower 1.4 GHz source surface density.

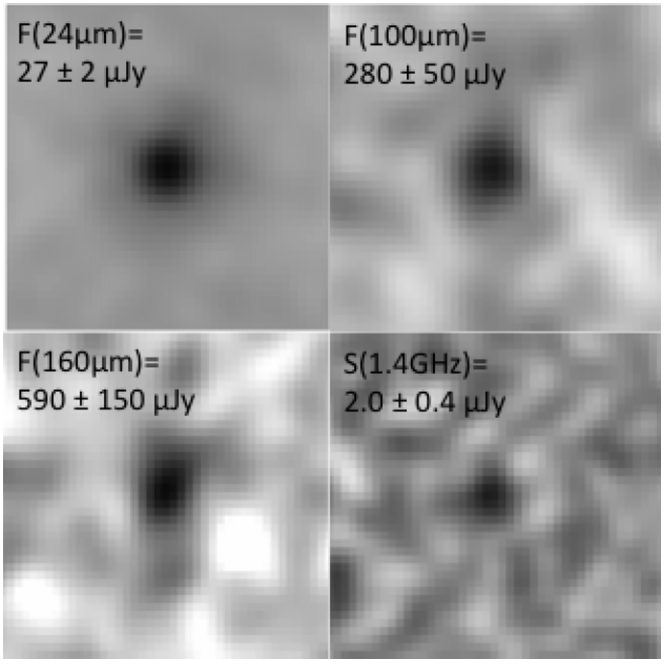

Figure 1. PSF-convolved median stacked images (≈25″ on a side) for "Sample B" (L^* galaxies) at 24, 100, 160 μm, and 1.4 GHz, with pixel scales of 1.″2, 1.″2, 2.″4, and 0.″5, respectively.

all optical, K_s-band, and IRAC detections in the GOODS-North field. The 3σ sensitivities, as measured in a 2″ diameter aperture in the optical and K_s-band images, are $\mathcal{R} \simeq 27.6$ and $K_s \simeq 24.55$. The 3σ sensitivities of the GOODS-North IRAC data, as measured in a 4″ diameter aperture, are 26.56, 26.00, 24.17, and 24.16, for the four IRAC channels, respectively. Any galaxies in our sample that lie within a distance $r_{\rm exc}$ of any source detected in the optical, near-IR, or with IRAC are excluded from the stack. The sample itself was selected such that galaxies that were confused with any nearby MIPS 24 μm sources were excluded.

The median 100 μm fluxes obtained with and without adopting an exclusion radius are listed in Table 1. The differences between these fluxes are smaller than the 1σ measurement uncertainties in the stacked fluxes. The similarity in flux between the exclusion and no-exclusion cases implies that any objects that may cluster around the UV-selected galaxies do not contribute significantly to the stacked far-infrared fluxes of the UV-selected galaxies. We note that there may exist very faint sources that are undetected in the optical, near-IR, and IRAC data and which may lie close to our targets. However, we consider it unlikely for sources that are faint at virtually all other wavelengths (optical, near-IR, and the *Spitzer* IRAC and MIPS bands) to be bright enough at 100 μm to contribute significantly to the stacked flux of the UV-selected galaxies. Performing a similar test at 160 μm is not possible, as the larger FWHM results in an exclusion radius that precludes any galaxies from being stacked. Because the 100 and 160 μm emission arises from the same mechanism (dust emission), then one would conclude that the effects of clustering are unlikely to be significant at 160 μm if the 100 μm stacked emission yields similar infrared luminosities to those obtained from the stacked 160 μm data. In Section 4, we present evidence that suggests that an additional contribution to the 160 μm flux from other sources must be negligible compared to the flux from the UV-selected galaxies of interest here. Based on this evidence, and to take advantage of all the galaxies in our sample, we proceed by adopting the

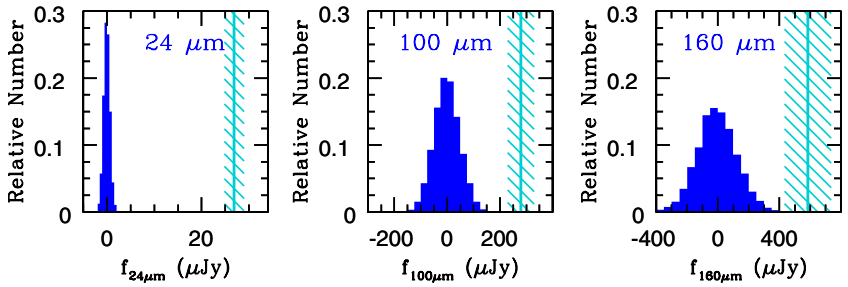

Figure 2. Comparison of measured stacked fluxes (mean and uncertainty indicated by the solid lines and hashed regions, respectively) for Sample B and the distribution of fluxes obtained by stacking on $N = 114$ random positions, repeated 10,000 times (histograms).

(A color version of this figure is available in the online journal.)

Table 2
Properties of the Stacks II: Summary of Mid-IR, IR, and Radio Fluxes

Sample	f_{24} (Jy)	f_{100} (Jy)	f_{160} (Jy)	$f_{1.4}$ (Jy)
A	$(33 \pm 4) \times 10^{-6}$	$(3.0 \pm 0.4) \times 10^{-4}$	$(7.3 \pm 1.2) \times 10^{-4}$	$(2.1 \pm 0.5) \times 10^{-6}$
B	$(27 \pm 2) \times 10^{-6}$	$(2.8 \pm 0.5) \times 10^{-4}$	$(5.9 \pm 1.5) \times 10^{-4}$	$(2.0 \pm 0.4) \times 10^{-6}$
C	$(21 \pm 3) \times 10^{-6}$	$(2.1 \pm 0.7) \times 10^{-4}$	$(5.4 \pm 1.6) \times 10^{-4}$	$(1.6 \pm 0.6) \times 10^{-6}$
D	$(35 \pm 3) \times 10^{-6}$	$(3.4 \pm 0.6) \times 10^{-4}$	$(6.6 \pm 2.1) \times 10^{-4}$	$(2.6 \pm 0.7) \times 10^{-6}$
E	$(130 \pm 4) \times 10^{-6}$	$(9.9 \pm 1.2) \times 10^{-4}$	$(22.4 \pm 3.8) \times 10^{-4}$	$(6.6 \pm 1.3) \times 10^{-6}$
F	$(10 \pm 2) \times 10^{-6}$	3σ: $< 3.2 \times 10^{-4}$	$(4.6 \pm 3.3) \times 10^{-4}$	3σ: $< 3.1 \times 10^{-6}$

Note. The quoted errors reflect measurement uncertainty in the stacked fluxes.

fluxes obtained without using the exclusion radius; these values are given in Table 2. Below, we discuss two additional tests used to verify these stacked fluxes.

3.3.2. Comparison with Random Stacks

The probability of a chance measurement that results in fluxes as high as the ones obtained by stacking on the positions of UV-selected galaxies (i.e., the target stacks) can be determined by stacking at random positions in the images (i.e., random stacks). We performed this random stack test on the radio and 24, 100, and 160 μm data (we did not exclude positions that correspond to detected sources). The results for the mid-IR and IR simulations for Sample B (stacking on $N = 114$ positions) are shown in Figure 2. For this sample, the 24 and 100 μm fluxes measured for 10,000 random stacks were never as high as those obtained for the target stacks. For the 160 μm data, 15 out of 10,000 random stacks result in fluxes that were within the 1σ measurement uncertainty of the target stack. The random stacks indicate a very low probability ($\lesssim$0.2%) of accidentally recovering stacked fluxes as high as the ones observed for the sample of L^* galaxies at $z \sim 2$, and these probabilities are consistent with those expected based on the measurement uncertainties of the stacked fluxes.

3.3.3. Stacks of Simulated Galaxies

Building on the random stack tests, point sources of known flux density were added at random locations in the residual images (using the same PSFs that are used to obtain photometry[22]) and were recovered by a stacking analysis. We added the same number of point sources to the residual images as are used in constructing the stacks for Samples A through E. Flux densities were assigned based on a Gaussian distribution with a mean equivalent to the median stacked flux for each sample (the stacks are insensitive to the dispersion in simulated fluxes). The ratio of the measured stack to simulated mean flux are shown in Figure 3 for the different samples, with numbers and input mean fluxes indicated, for the 24, 100, and 160 μm data. This ratio is close to but not exactly equal to 1, with a bias of just a few percent. The biases and dispersions measured for the different stacks are summarized in Table 3. The error in the mean recovered stacked flux from the simulations is much smaller than the measurement uncertainty. Therefore, for the subsequent discussion we assume a flux uncertainty that is equal to the measurement uncertainty of the stacked flux. Finally, we corrected the observed fluxes (listed in Table 2) by the bias factors given in Table 3 before inferring the total infrared luminosities, as we discuss in the next section.

Table 3
Properties of the Stacks III: Biases and Errors in Stacked Fluxes

Sample	24 μm 1-Bias[a]/Error[b]	100 μm 1-Bias[a]/Error[b]	160 μm 1-Bias[a]/Error[b]	1.4 GHz 1-Bias[a]/Error[b]
A	0.94/0.002	0.96/0.012	0.92/0.014	1.03/0.016
B	0.94/0.003	0.95/0.017	0.92/0.022	1.02/0.024
C	0.94/0.015	0.96/0.039	0.92/0.040	1.03/0.054
D	0.94/0.004	0.96/0.035	0.92/0.045	1.03/0.038
E	0.95/0.009	0.95/0.046	0.93/0.058	1.05/0.075

Notes.
[a] Average bias of stacked flux, defined as the ratio of the mean measured flux to the simulated flux, $\langle f^{\rm meas} \rangle / f^{\rm sim}$.
[b] Fractional uncertainty in the mean stacked flux, taken as the ratio of the error in the mean of the measured stacked flux ($\sigma/\sqrt{N}$) to the median measured flux, i.e., $\sigma(f^{\rm meas})/(\sqrt{N}\langle f^{\rm meas} \rangle)$.

[22] We performed another test to determine if asymmetries in the intrinsic *Herschel* PSF result in systematic differences in the photometry obtained for simulated sources. For this test, we redid the simulations by adding point sources of known flux density, where we assumed the flux profile given by the PACS PSF measured by observing the asteroid Vesta. The sources were then recovered using the PSF measured from the GOODS-N *Herschel* images. Based on this second set of simulations, we find less than 5% systematic offset between the difference of input and output flux relative to the difference obtained when assuming the same PSF, both for adding sources to the images and recovering their fluxes.

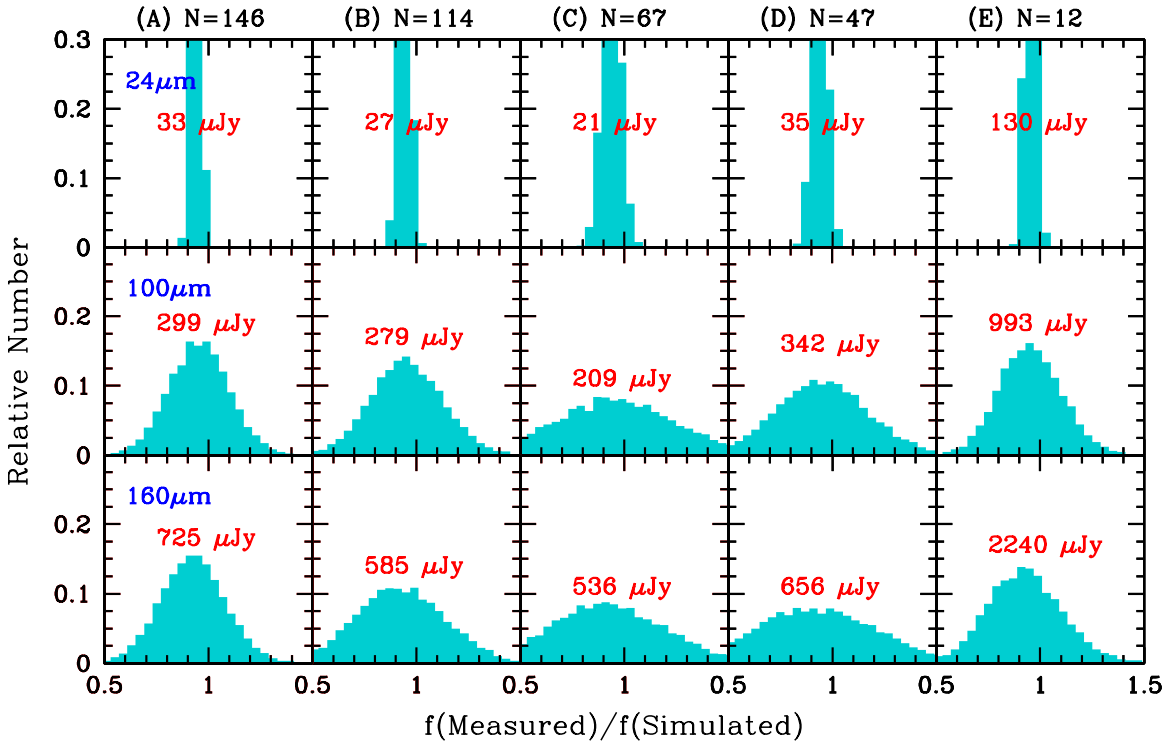

Figure 3. Distribution of stacked fluxes for artificial galaxies added to the 24, 100, and 160 μm images (histograms) for Samples A through E, relative to the simulated flux (numbers in panels).

(A color version of this figure is available in the online journal.)

3.3.4. Summary of Tests

We have performed several tests to validate our measures of the stacked fluxes for UV-selected galaxies. The method employed here is able to recover the stacked fluxes of galaxies with a bias of just a few percent relative to the known fluxes of artificial sources added to the 1.4 GHz, and 24, 100, and 160 μm images. These tests also imply a very low probability ($\lesssim$0.2%) of accidentally recovering stacked fluxes that are as high as the target stacked fluxes. Finally, we test for the effect of source clustering on the stacked flux at 100 μm. By excluding galaxies from the stack which have any nearby sources, we find that the remaining galaxies have a median flux that is identical within the measurement errors of the median flux inferred for the entire sample of galaxies. This indicates that any sources that may cluster around the UV-selected galaxies (if they exist) do not affect the stacking results.

4. INFRARED LUMINOSITIES AND DUST SEDs

4.1. Dust SED Templates and Extrapolation to the Radio

To infer the total infrared luminosities L(8–1000 μm) $\equiv L_{\rm IR}$ of the $z \sim 2$ galaxies, we employed several publicly available dust SED templates including those of Chary & Elbaz (2001, hereafter CE01), Dale & Helou (2002, hereafter DH02), and Rieke et al. (2009, hereafter Rieke+09). We also include the median templates presented in Elbaz et al. (2011). Specifically, these authors define an "infrared main sequence" of galaxies, where the ratio of $L_{\rm IR}$ to L_8 (IR8) is universal for most star-forming galaxies at $z \lesssim 2.0$, having a value of $L_{\rm IR}/L_8 = 4.9^{+2.9}_{-2.2}$. The "infrared starbursts" are considered to be those galaxies with IR8 ratios in excess of $\approx$15. Elbaz et al. (2011) demonstrate that variations in IR8 may be due primarily to differences in the infrared luminosity surface density of galaxies, such that main-sequence galaxies are characterized by star formation that is more extended than that present in starbursts (see Section 5). We fit the median IR SED of these main-sequence ("Elbaz+11-MS") and starburst galaxies ("Elbaz+11-SB") to the stacked fluxes.

The Reddy et al. (2010) calibration between rest-frame 8 μm emission and infrared luminosity is considered as well. In this case, L_8 is computed by k-correcting the 24 μm flux using the average of 12 local galaxy mid-IR SEDs specified in Reddy et al. (2006b). The correlation between L_8 and Hα luminosity is then used to infer the L_8–$L_{\rm IR}$ conversion, based on using Hα as an independent probe of the star formation (Reddy et al. 2010). Finally, we make use of the radio–infrared (IR) correlation to provide an independent estimate of $L_{\rm IR}$, assuming that this relation does not evolve with redshift, as is consistent with the evidence, at least at redshifts $z \lesssim 3$ (e.g., Appleton et al. 2004; Ivison et al. 2010; Sargent et al. 2010; Bourne et al. 2011; Mao et al. 2011). For the subsequent analysis, we use the radio–IR correlation published in Bell (2003). The sample of Yun et al. (2001) is roughly a factor of 10 larger than the one analyzed by Bell (2003). However, Yun et al. (2001) calibrate the 60 μm luminosity, L_{60}, with radio luminosity, and the former requires some assumption about the relation between L_{60} and $L_{\rm IR}$. To make the minimum number of assumptions, we therefore adopted the Bell (2003) calibration which directly relates the total infrared luminosities to the specific luminosity at 1.4 GHz.

The CE01 and Rieke+09 models are parameterized such that we can relate any template to a given total infrared luminosity. The Elbaz+11-MS/SB templates are normalized to an infrared luminosity of $L_{\rm IR} = 10^{11}\ L_{\odot}$. The DH02 models are presented as a function of radiation field intensity and, following the literature (e.g., Papovich et al. 2007), we associate infrared

luminosities with each of the DH02 templates assuming the empirical calibration of Marcillac et al. (2006). The CE01 and Rieke+09 models also include an extrapolation to radio wavelengths by assuming some version of the local radio-far-IR correlation (Condon 1992; Yun et al. 2001; Bell 2003). For a consistent treatment, we have adjusted the models (or added to them, in the case of DH02 and Elbaz+11-MS/SB) for a radio spectrum with index $\gamma = -0.8$ (Condon 1992), normalized to have a specific luminosity at 1.4 GHz corresponding to the $L_{\rm IR}$ for that template, assuming the Bell (2003) calibration.

4.2. Fitting Procedure

Because the far-infrared peak of the dust emission in the SED templates shifts to shorter wavelengths at higher luminosities, we can either (1) fit these templates directly to the observed infrared and radio fluxes ("luminosity-matched" fitting) or (2) find the template that best matches the infrared colors and then normalize this template to the observed fluxes ("color-matched" fitting). The color-matched fitting yields larger uncertainties in $L_{\rm IR}$ because the color errors are larger than those for individual flux measurements. We have adopted both methods for comparison purposes. The Elbaz+11-MS/SB templates are based on the composite IR SED of the "main-sequence" and "starburst" galaxy samples of Elbaz et al. (2011), and are normalized to $L_{\rm IR} = 10^{11}\,L_{\odot}$. We assume the same spectral shape (i.e., no color dependence) when fitting these templates to the observed fluxes. Further, in finding the best-fit template, we include results where all fluxes have been weighted equally, as well as being weighted by their errors. The equal weighting is done to ensure that the higher signal-to-noise ratio (S/N) 24 μm data (and thus the smaller measurement uncertainties at 24 μm) do not unduly skew the template fits.

4.3. Infrared Luminosities

Table 4 lists the $L_{\rm IR}$ corresponding to the best-fit templates for different combinations of the stacked fluxes for Samples A through F, after taking into account the biases and dispersions in these fluxes (see discussion above and Table 3). The errors in $L_{\rm IR}$ are based on the measurement uncertainties in the stacked fluxes. The fact that we are stacking on galaxies over a relatively wide range of redshifts ($1.5 \leqslant z < 2.6$) introduces an additional 30% scatter in the derived $L_{\rm IR}$. Fitting for different combinations of the infrared and radio data allows us to determine if the inclusion of any of the stacked fluxes results in significant changes in the inferred infrared luminosities. Also included in this table are the results from using the Reddy et al. (2010) calibration between L_8 and $L_{\rm IR}$, and the $L_{\rm IR}$ corresponding radio luminosity assuming the Bell (2003) radio–IR correlation.

The systematic uncertainties in $\log(L_{\rm IR})$ for the different combinations of templates, fluxes, and fitting methods for each of the subsamples are typically within 0.1 dex. We note that the $L_{\rm IR}$ derived from 160 μm is not systematically larger than that inferred from 100 μm, and hence runs counter to what one might expect if the larger 160 μm beam included more sources clustered around the UV-selected galaxies that contribute to the measured far-infrared flux. The stacked radio data have significantly higher resolution ($\sim$1.″7 at 1.4 GHz versus $\sim$11″ at 160 μm) and yield a radio flux that implies an $L_{\rm IR}$ that is also not any smaller than the value inferred from the 160 μm data. Based on this evidence, we conclude that the 160 μm emission from sources proximate to the UV-selected galaxies is negligible compared to the emission from the UV-selected galaxies themselves.

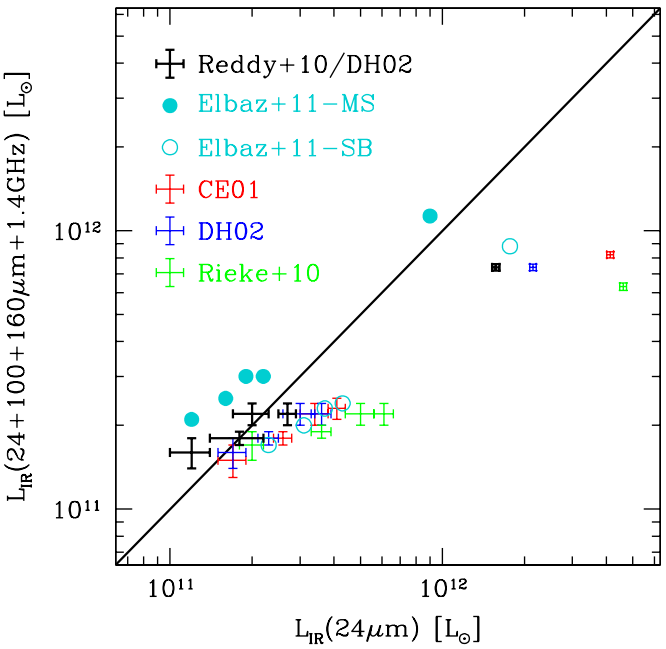

Figure 4. Comparison between the $L_{\rm IR}$ computed from the 24, 100, 160 μm, and 1.4 GHz equally weighted fluxes, and the $L_{\rm IR}$ computed from the 24 μm data only. The heavy black points denote the $L_{\rm IR}$ computed from the Reddy et al. (2010) calibration vs. the $L_{\rm IR}$ obtained from the best-fit DH02 template that includes all the data (24, 100, 160 μm, and 1.4 GHz), equally weighted. Error bars reflect the uncertainty in the $L_{\rm IR}$ inferred from the stacked measurements, except for the high-luminosity subsample (Sample E), where the errors include the intrinsic dispersion in 24 μm fluxes of objects that contribute to the sample. For clarity, error bars are not shown for the Elbaz+11-MS/SB points.

(A color version of this figure is available in the online journal.)

The notable outliers listed in Table 4 are the $L_{\rm IR}$ determined from 24 μm flux density alone, which tend to overpredict $L_{\rm IR}$, particularly for the highest luminosity subsamples D and E, relative to cases where we include the 100 and 160 μm data in most of the template fits (Figure 4). Alternatively, with the Elbaz+11-MS template, 24 μm only determinations result in systematically lower $L_{\rm IR}$. These differences are due to the intrinsic variation in the ratio of L_8 to $L_{\rm IR}$ luminosity present in the templates relative to the observed SED. The systematic overestimation of $L_{\rm IR}$ based on L_8 alone has been noted before for ULIRGs studied with *Spitzer* (Papovich et al. 2007, 2009; Daddi et al. 2007; Murphy et al. 2011; Magnelli et al. 2011) and *Herschel* (Nordon et al. 2010; Elbaz et al. 2010). For the samples considered here, the same 24 μm bias is apparent for all templates (except for Elbaz+11-MS) even at luminous infrared galaxy (LIRG) luminosities, where the difference between the best-fit $L_{\rm IR}$ and that determined from 24 μm alone is similar to the 1σ uncertainties in $L_{\rm IR}$.

Using *Spitzer* and *Herschel* data for galaxies at redshifts $z \lesssim 2.0$, Elbaz et al. (2011) investigate the physical reasons for the overestimation of $L_{\rm IR}$ based on rest-frame L_8 alone. These authors point out that the SED templates used to infer $L_{\rm IR}$ are calibrated to match local ULIRGs, which are starbursts with compact, high surface density star formation. This contrasts with ULIRGs at high redshift ($z \gtrsim 2.0$) which have more extended star formation occurring over longer timescales. These differences in star formation surface densities and timescales lead to noticeable differences in the IR SEDs because of the variations in the spatial distribution of dust with respect to the massive stars that are heating this dust. In Section 5, we discuss the $L_{\rm IR}/L_8$ ratios found here and place them in the context

Table 4
Comparison of Infrared Luminosities (L_{IR})[a]

Template	λ, ν[b]	Sample A	Sample B	Sample C	Sample D	Sample E	Sample F
R10a[c]	24	2.0 ± 0.3	1.8 ± 0.1	1.2 ± 0.2	2.7 ± 0.2	15.7 ± 0.5	0.3 ± 0.1
Bell03[d]	1.4	2.2 ± 0.5	2.2 ± 0.4	1.7 ± 0.6	2.9 ± 0.8	7.9 ± 1.7	3σ: < 3.0
Elbaz+11-MS Lum[e]	24	1.9 ± 0.2	1.6 ± 0.1	1.2 ± 0.1	2.2 ± 0.2	9.0 ± 0.3	0.5 ± 0.1
...	100	3.0 ± 0.4	2.9 ± 0.5	2.0 ± 0.6	3.8 ± 0.7	12.7 ± 1.4	3σ: < 2.8
...	160	3.0 ± 0.4	2.4 ± 0.6	2.1 ± 0.6	2.9 ± 0.9	11.1 ± 1.7	1.7 ± 1.1
...	100, 160	3.0 ± 0.3	2.7 ± 0.4	2.1 ± 0.4	3.5 ± 0.5	12.0 ± 1.0	3σ: < 2.8
...	24, 100, 160	2.3 ± 0.3	1.7 ± 0.2	1.3 ± 0.2	2.3 ± 0.3	9.2 ± 0.4	3σ: < 2.8
...	24, 100, 160, 1.4	2.3 ± 0.3	1.7 ± 0.2	1.3 ± 0.2	2.3 ± 0.3	9.2 ± 0.5	3σ: < 2.8
Elbaz+11-MS Lum-Eq Weight[f]	24, 100, 160, 1.4	3.0 ± 0.2	2.5 ± 0.2	2.1 ± 0.2	3.0 ± 0.2	11.3 ± 0.3	3σ: < 2.8
Elbaz+11-SB Lum[e]	24	3.7 ± 0.5	3.1 ± 0.2	2.3 ± 0.3	4.3 ± 0.4	17.7 ± 0.5	1.0 ± 0.2
...	100	2.4 ± 0.3	2.3 ± 0.4	1.6 ± 0.5	3.0 ± 0.5	10.0 ± 1.1	3σ: < 2.2
...	160	2.3 ± 0.3	1.9 ± 0.5	1.7 ± 0.5	2.3 ± 0.7	8.6 ± 1.3	1.3 ± 0.9
...	100, 160	2.4 ± 0.2	2.1 ± 0.3	1.6 ± 0.3	2.7 ± 0.4	9.4 ± 0.9	3σ: < 2.2
...	24, 100, 160	2.6 ± 0.3	2.7 ± 0.3	2.0 ± 0.3	3.6 ± 0.4	15.5 ± 0.7	3σ: < 2.2
...	24, 100, 160, 1.4	2.6 ± 0.4	2.6 ± 0.3	2.0 ± 0.4	3.5 ± 0.5	15.0 ± 0.8	3σ: < 2.2
Elbaz+11-SB Lum-Eq Weight[f]	24, 100, 160, 1.4	2.3 ± 0.2	2.0 ± 0.1	1.7 ± 0.2	2.4 ± 0.2	8.8 ± 0.2	3σ: < 2.2
CE01 Lum[e]	24	3.4 ± 0.4	2.6 ± 0.2	1.7 ± 0.2	4.1 ± 0.3	41.3 ± 1.2	0.4 ± 0.1
...	100	2.4 ± 0.3	2.3 ± 0.4	1.6 ± 0.5	3.1 ± 0.6	10.9 ± 1.2	3σ: < 2.3
...	160	2.2 ± 0.3	1.8 ± 0.4	1.5 ± 0.4	2.1 ± 0.6	7.9 ± 1.2	1.2 ± 0.8
...	100, 160	2.3 ± 0.3	2.0 ± 0.3	1.6 ± 0.3	2.7 ± 0.4	9.4 ± 0.9	3σ: < 2.3
...	24, 100, 160	2.4 ± 0.3	2.3 ± 0.3	1.6 ± 0.3	3.3 ± 0.4	12.3 ± 0.4	3σ: < 2.3
...	24, 100, 160, 1.4	2.4 ± 0.4	2.3 ± 0.3	1.6 ± 0.4	3.2 ± 0.4	12.1 ± 0.6	3σ: < 2.3
CE01 Lum-Eq Weight[f]	24, 100, 160, 1.4	2.2 ± 0.2	1.8 ± 0.1	1.5 ± 0.2	2.3 ± 0.2	8.2 ± 0.2	3σ: < 2.3
CE01 Col[g]	100, 160	2.1 ± 0.4	1.8 ± 0.5	2.1 ± 1.0	1.7 ± 0.6	7.9 ± 1.5	...
...	24, 100, 160	2.3 ± 0.6	2.2 ± 0.8	1.6 ± 0.9	3.0 ± 1.2	10.4 ± 2.3	...
CE01 Col-Eq Weight[h]	24, 100, 160, 1.4	2.4 ± 0.7	2.2 ± 0.8	1.6 ± 0.9	3.0 ± 1.2	12.1 ± 2.7	...
DH02 Lum[e]	24	3.0 ± 0.4	2.3 ± 0.2	1.7 ± 0.2	3.6 ± 0.3	21.5 ± 0.6	0.6 ± 0.1
...	100	2.1 ± 0.3	2.0 ± 0.4	1.5 ± 0.5	2.7 ± 0.5	7.8 ± 0.9	3σ: < 2.0
...	160	2.2 ± 0.3	1.8 ± 0.4	1.6 ± 0.4	2.1 ± 0.6	7.4 ± 1.2	1.3 ± 0.9
...	100, 160	2.1 ± 0.2	1.9 ± 0.2	1.5 ± 0.3	2.5 ± 0.4	7.7 ± 0.6	3σ: < 2.0
...	24, 100, 160	2.3 ± 0.3	2.2 ± 0.2	1.6 ± 0.2	3.0 ± 0.4	13.6 ± 0.7	3σ: < 2.0
...	24, 100, 160, 1.4	2.3 ± 0.3	2.2 ± 0.3	1.6 ± 0.3	3.0 ± 0.5	13.2 ± 0.8	3σ: < 2.0
DH02 Lum-Eq Weight[f]	24, 100, 160, 1.4	2.2 ± 0.2	1.8 ± 0.1	1.6 ± 0.2	2.2 ± 0.2	7.4 ± 0.2	3σ: < 2.0
DH02 Col[g]	100, 160	2.2 ± 0.4	1.5 ± 0.5	1.7 ± 0.7	1.7 ± 0.6	6.9 ± 1.3	...
...	24, 100, 160	2.4 ± 0.7	2.1 ± 0.7	1.5 ± 0.8	2.8 ± 1.1	10.5 ± 2.4	...
DH02 Col-Eq Weight[h]	24, 100, 160, 1.4	2.3 ± 0.6	2.2 ± 0.8	1.6 ± 0.9	3.6 ± 1.5	9.5 ± 2.2	...
Rieke+09 Lum[e]	24	5.0 ± 0.6	3.6 ± 0.3	2.0 ± 0.2	6.1 ± 0.5	46.1 ± 1.3	0.5 ± 0.1
...	100	2.5 ± 0.3	2.3 ± 0.4	1.8 ± 0.6	3.0 ± 0.5	8.2 ± 0.9	3σ: < 2.3
...	160	2.2 ± 0.3	1.9 ± 0.4	1.7 ± 0.5	2.1 ± 0.6	6.1 ± 0.9	1.4 ± 1.0
...	100, 160	2.3 ± 0.2	2.1 ± 0.2	1.7 ± 0.2	2.5 ± 0.3	7.1 ± 0.6	3σ: < 2.3
...	24, 100, 160	2.3 ± 0.2	2.3 ± 0.3	1.8 ± 0.3	3.1 ± 0.4	11.2 ± 0.7	3σ: < 2.3
...	24, 100, 160, 1.4	2.3 ± 0.3	2.3 ± 0.3	1.8 ± 0.4	3.0 ± 0.5	11.0 ± 0.9	3σ: < 2.3
Rieke+09 Lum-Eq Weight[f]	24, 100, 160, 1.4	2.2 ± 0.2	1.9 ± 0.1	1.7 ± 0.2	2.2 ± 0.2	6.3 ± 0.2	3σ: < 2.3
Rieke+09 Col[g]	100, 160	3.1 ± 0.6	2.8 ± 0.8	2.4 ± 1.3	3.6 ± 1.3	12.5 ± 2.7	...
...	24, 100, 160	2.7 ± 0.7	2.4 ± 0.8	1.8 ± 1.0	3.2 ± 1.3	11.9 ± 2.7	...
Rieke+09 Col-Eq Weight[h]	24, 100, 160, 1.4	2.6 ± 0.7	2.3 ± 0.8	1.8 ± 0.9	3.1 ± 1.2	12.1 ± 2.7	...

Notes.
[a] Luminosities are in units of 10^{11} $L_{\odot}$. Errors in luminosities are derived from the uncertainties in the stacked fluxes (see the text).
[b] Wavelengths (in micron) or frequency (in GHz) used to compute the best-fit L_{IR}.
[c] L_{IR} determined from the calibration of 24 μm with L_{IR} of Reddy et al. (2010), which is based upon the correlation between 8 μm and Hα luminosity for L^* galaxies at $z \sim 2$.
[d] L_{IR} determined from the radio–IR correlation of Bell (2003), and assuming a radio spectral slope of $\gamma = -0.8$.
[e] L_{IR} for the Elbaz et al. (2011) main sequence/starburst, Chary & Elbaz (2001), Dale & Helou (2002), or Rieke et al. (2009) template that best matches the observed fluxes (weighted by the flux errors), irrespective of the infrared colors.
[f] L_{IR} for the Elbaz et al. (2011) main sequence/starburst, Chary & Elbaz (2001), Dale & Helou (2002), or Rieke et al. (2009) template that best matches the observed fluxes (including 1.4 GHz), with all fluxes given equal weight in the fitting, irrespective of the infrared colors.
[g] L_{IR} for the Chary & Elbaz (2001), Dale & Helou (2002), or Rieke et al. (2009) template that best fits the observed infrared colors and is normalized to match the observed fluxes, with colors and fluxes weighted by their errors.
[h] L_{IR} for the Chary & Elbaz (2001), Dale & Helou (2002), or Rieke et al. (2009) template that best fits the observed infrared colors and is normalized to match the observed fluxes (including 1.4 GHz), with colors and fluxes weighted equally.

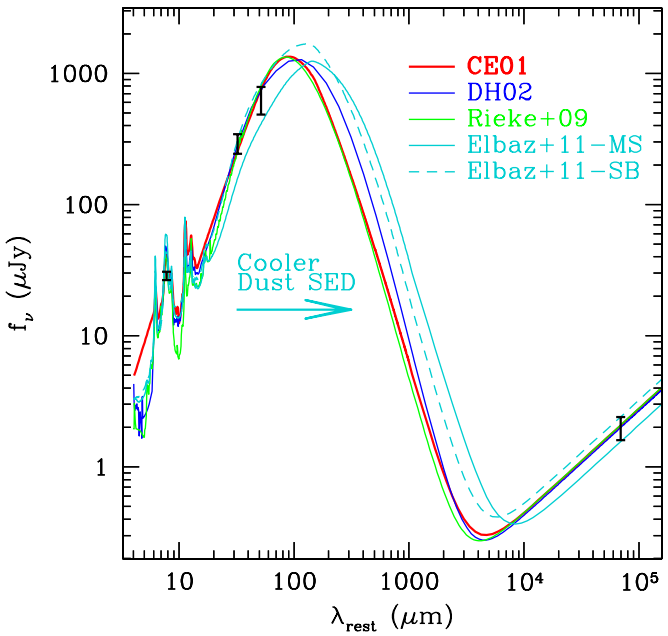

Figure 5. Comparison of the Chary & Elbaz (2001), Dale & Helou (2002), Rieke et al. (2009), and Elbaz et al. (2011) main-sequence and starburst template fits to the observed 24, 100, and 160 μm and 1.4 GHz measurements, derived by scaling the template that best matches the observed infrared colors, for L^* galaxies at $z \sim 2$. The total infrared luminosities for the different templates are identical within the uncertainties (Table 4).

(A color version of this figure is available in the online journal.)

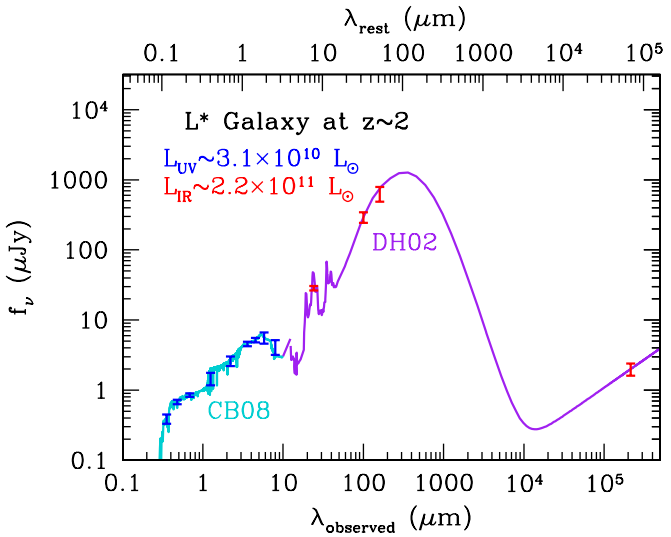

Figure 6. Best-fit stellar population (CB08) and dust (DH02) SEDs for typical L^* galaxies at $z \sim 2$. Included are $U_nG\mathcal{R}JK_s$, *Spitzer*/IRAC 3.6–8.0 μm, *Spitzer* MIPS 24 μm, *Herschel*/PACS 100 and 160 μm, and VLA 1.4 GHz stacked measurements.

(A color version of this figure is available in the online journal.)

of the ratios found for other star-forming galaxies with similar luminosities but at lower redshifts.

We conclude by noting that the Reddy et al. (2010) calibration, which is based on the correlation between L_8 and dust-corrected Hα luminosity at $z \sim 2$, predicts L_{IR} for LIRGs that are similar within the errors to those computed using the combined *Spitzer*, *Herschel*, and VLA data. Finally, the infrared luminosities based on the radio data alone are in excellent agreement with the infrared luminosities inferred from fitting the dust templates to the observed 24, 100, and 160 μm fluxes.

4.4. Comparison of Dust SEDs

Figure 5 compares the dust SEDs found for the luminosity-matched fitting to the 24, 100, and 160 μm, and 1.4 GHz data, weighted by their errors. The dust SEDs for the different models are broadly consistent with each other; one difference is in the stronger silicate absorption at 9 μm and additional aromatic features longward of 10 μm in the Rieke+09 model fit. The Rieke+09 templates are calibrated using *Spitzer*/IRS (InfraRed Spectrograph) spectra, rather than photometry, between 5 and 36 μm, and will understandably include mid-IR spectral features that are not present in the other models.

The most notable difference between the templates can be seen in Figure 5: the Elbaz+11 and DH02 templates exhibit a broader range of dust temperatures with a colder dust component, relative to CE01 and Rieke+09. Resolving the full shape of the SED, and the average dust temperatures, will require larger stacked samples and deeper data in the submillimeter and millimeter regime. In any case, while some obvious differences remain between the model templates given the data at our disposal, the integrals of these SEDs, namely the total L_{IR}, are essentially identical within the uncertainties (Table 4). For the subsequent analysis, we assume the L_{IR} determined from the DH02 model that best fits the error-weighted fluxes at 1.4 GHz, 24, 100, and 160 μm. Assuming the L_{IR} derived using any of the other models does not affect our conclusions.

4.5. The Dust SED of Typical Star-forming Galaxies at $z \sim 2$

The average stellar population and dust SEDs for L^*_{UV} galaxies at $z \sim 2$ are shown in Figure 6. The optical photometry indicates that an L^*_{UV} galaxy at $z \sim 2$ has a UV luminosity of $L_{UV} \simeq 3.1 \times 10^{10}\ L_\odot$ and the dust SED indicates a total infrared luminosity of $L_{IR} \simeq 2.2 \times 10^{11}\ L_\odot$. The *Herschel* and VLA data confirm the previous finding that UV-selected galaxies at $z \sim 2$ with $\mathcal{R} < 25.5$ are LIRGs (Reddy et al. 2005, 2006b, 2010; Adelberger & Steidel 2000); in particular, the median L_{IR} found here is virtually identical to that found by Reddy et al. (2010) based on an analysis of the 24 μm, Hα, and UV emission for UV-selected galaxies at $z \sim 2$. We also point out that the median value of L_{IR} for L^*_{UV} galaxies is similar (to within a factor of $\approx$3) to the value of L^*_{IR} deduced from direct *Spitzer* determinations of the IR LF at $z \sim 2$ (Magnelli et al. 2011).

The necessity of stacking the UV-selected galaxies, even for GOODS-depth *Herschel*/PACS data, is illustrated in Figure 7. Typical L^* galaxies at $z \sim 2$ are easily detected at wavelengths blueward of observed 24 μm given the depths of the data considered here. Redward of this point, however, the dust emission is not sufficient for directly detecting these galaxies, thus stacking in the infrared and radio bands is required. Fortunately, the *Herschel*/PACS sensitivity and resolution are such that we can for the first time significantly detect the average thermal emission of non-lensed L^* galaxies at $z \sim 2$.

4.6. Variation of L_{IR} with UV Slope and Bolometric Luminosity

The stacks for the different subsamples indicate that galaxies with bluer UV spectral slopes are on average less infrared luminous than those with red UV spectral slopes (Table 4). This systematic effect is approximately equal in magnitude to the uncertainties in the stacked flux measurements. Not surprisingly, those galaxies that are inferred to have $L_{bol} \geqslant 10^{12}\ L_\odot$ based on the MIPS 24 μm data (Sample E, Table 4) have median stacked fluxes at 100 and 160 μm that are a factor of 3–4 times larger

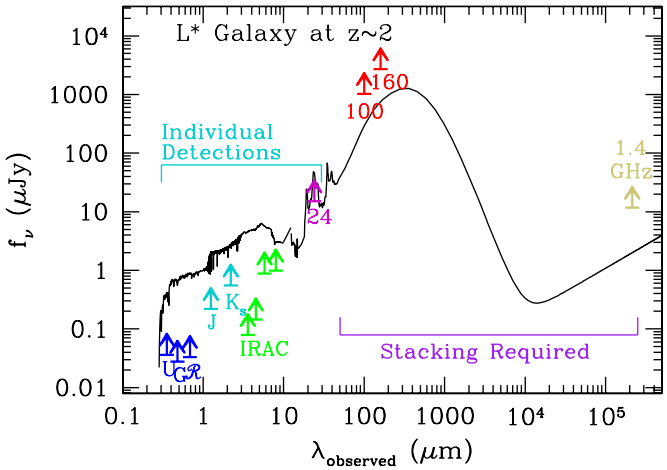

Figure 7. Detections limits (3σ) for the ground-based optical ($U_nG\mathcal{R}$), ground-based near-IR (JK_s), *Spitzer*/IRAC (3.6–8.0 μm), *Spitzer*/MIPS (24 μm), *Herschel*/PACS (100, 160 μm), and VLA 1.4 GHz data in the GOODS-North field, relative to the SED of an L^* galaxy at $z \sim 2$.

(A color version of this figure is available in the online journal.)

than the corresponding fluxes for the L^* sample. The median infrared luminosity for Sample E is not as large as that computed from 24 μm alone and hence not as large as the value of $L_{\rm bol}$ used to construct this subsample (e.g., Figure 4). However, the best-fit template to the mid-IR, IR, and radio fluxes indicates that galaxies in Sample E are still more infrared luminous than galaxies in other subsamples. These galaxies correspond to low-luminosity ULIRGs or higher luminosity LIRGs. In the next section, we compare the infrared and UV luminosities for each of the subsamples of UV-selected galaxies.

5. DISCUSSION

In the following, we discuss our results on L^* galaxies at $z \sim 2$ in the context of the infrared properties of star-forming galaxies with similar luminosities at lower redshifts. We then discuss the combined UV and IR luminosity measurements for $z \sim 2$ galaxies and the implication for their average dust attenuation. We also compare the measured dust attenuation with that inferred from the local correlation between dustiness and UV slope. Finally, we use the *Herschel* data to determine the median bolometric luminosities and SFRs of galaxies in our sample, the correlation between bolometric luminosity and dust attenuation, and the variation in dust attenuation with UV luminosity.

5.1. Ratio of Infrared to Mid-infrared Luminosity

For a consistent comparison with Elbaz et al. (2011), we have recomputed L_8 using the mid-IR SED of M82 to k-correct the 24 μm flux. The implied k-corrections are not substantially different than those obtained from the average mid-IR SED of the 12 local star-forming galaxies listed in Reddy et al. (2006b). Adopting the CE01 luminosity matched and weighted value of $L_{\rm IR}$, we compute IR8 $= 7.7 \pm 1.6, 8.9 \pm 1.3, 8.3 \pm 2.4, 8.9 \pm 1.4$, and 8.4 ± 0.5, for Samples A, B, C, D, and E, respectively. Assuming the $L_{\rm IR}$ computed from the 100 and 160 μm data only results in ratios that are not significantly different than the ones quoted above. These values imply that the galaxies in our sample predominantly lie on the boundary between the ratios found for infrared main-sequence galaxies (IR8 $= 4.9^{+2.9}_{-2.2}$) and those found for starburst galaxies which have an exponential tail distribution extending to IR8 = 15–20. The relatively high IR8 ratios also may explain why the typically adopted templates (e.g., CE01) tend to not fail as badly for galaxies in our sample relative to more luminous ULIRGs at $z \sim 2$ when inferring $L_{\rm IR}$ from L_8 alone (e.g., Reddy et al. 2006b, 2010).

A detailed comparison between the morphologies of the $z \sim 2$ galaxies studied here and local star-forming galaxies is beyond the scope of this paper. However, we can still make some general inferences regarding the degree of "compactness" of the IR emission in these galaxies and how it may affect their IR8 ratios. We compute the IR luminosity surface density following Elbaz et al. (2011):

$$\Sigma_{\rm IR} \equiv \frac{L_{\rm IR}/2}{\pi r_{\rm IR}^2}. \quad (1)$$

The typical UV half-light radius of galaxies in our sample is $r_{\rm UV} \simeq 2$ kpc. If we assume that the IR half-light radius is roughly half this value, as suggested by Elbaz et al. (2011), then $r_{\rm IR} \approx 1$ kpc, implying $\Sigma_{\rm IR} \approx 3 \times 10^{10}\, L_\odot$ kpc^{-2}. On the other hand, if $r_{\rm IR} \approx r_{\rm UV}$ as might be expected for galaxies at high redshift where the UV emission is dominated by OB stars, then $\Sigma_{\rm IR} \approx 8 \times 10^9\, L_\odot$ kpc^{-2}. Even this lower value is a factor of four larger than the $\Sigma_{\rm IR} \lesssim 2 \times 10^9\, L_\odot$ kpc^{-2} typical of the infrared main-sequence galaxies with extended star formation in the Elbaz et al. (2011) sample. The relevance for the present discussion is that while L^* galaxies at $z \sim 2.3$ appear to have IR8 ratios that are a factor of $\approx$2 larger than for main-sequence galaxies at lower redshifts, they may also exhibit $\Sigma_{\rm IR}$ that are larger than those found for main-sequence galaxies, and hence are more compact for their IR luminosity. Formally, galaxies in our sample would lie on the "boundary" between IR main-sequence and IR starburst galaxies. Ultimately, more robust measurements of the IR sizes of galaxies in our sample will be needed for a fairer comparison to those presented in Elbaz et al. (2011) (e.g., the UV and IR sizes may be substantially different depending on the relative geometry of dust and stars). In any case, the larger IR8 ratio for the $z \sim 2$ sample results in the overprediction of $L_{\rm IR}$ based on L_8 alone when using the standard templates, as noted in Section 4.

One possibility is that the IR8 ratio for typical star-forming (L^*) galaxies may evolve with redshift, transitioning from IR8 $\simeq 4.9$ at $z \lesssim 2.0$ to IR8 $\simeq 8$ at $z \sim 2.3$. This effect may due to the smaller sizes of high-redshift galaxies for their IR luminosities relative to lower redshift galaxies. Finally, it is worth noting that the SFR surface density appears to be roughly constant for L^* galaxies at higher redshifts ($z \sim 4$–7; $\Sigma_{\rm SFR} \simeq 1.9\, M_\odot$ yr^{-1} kpc^{-2}; e.g., Oesch et al. 2010), suggesting that there may be a similar commonality in the IR8 ratios (if one could measure them) for typical star-forming galaxies at very high redshift, just as is observed for main-sequence galaxies at $z \lesssim 2.0$ (Elbaz et al. 2011).

5.2. Dust Obscuration of Typical Star-forming Galaxies at $z \sim 2$

5.2.1. Definitions Relevant to Dust Obscuration

Before proceeding, it is useful to define several terms that have been typically used interchangeably in the literature. First, we define "dust obscuration," or attenuation, as $L_{\rm IR}/L_{\rm UV}$. Note that this ratio is not equivalent to the ratio of obscured to unobscured SFR, $\rm SFR_{IR}/SFR_{UV}$, given the difference in scaling required to convert the UV and IR luminosities to SFRs. We also define the "dust correction factor" needed to recover the total SFR

Table 5
Properties of the Stacks IV: Derived Quantities

Sample	L_{UV}[a] ($10^{11}\,L_\odot$)	L_{IR}[b] ($10^{11}\,L_\odot$)	1+SFR(IR)/SFR(UV)[c,d]	SFR(UV)+SFR(IR)[d] ($M_\odot$ yr^{-1})
A	0.32 ± 0.02	2.3 ± 0.3	5.3 ± 0.6	49 ± 6
B	0.31 ± 0.02	2.2 ± 0.3	5.2 ± 0.6	47 ± 6
C	0.33 ± 0.03	1.6 ± 0.3	3.9 ± 0.6	37 ± 6
D	0.28 ± 0.02	3.0 ± 0.5	7.2 ± 1.1	60 ± 9
E	0.35 ± 0.07	13.2 ± 0.8	20.9 ± 3.2	238 ± 15.5
F	0.38 ± 0.05	3σ: < 2.0	3σ: < 2.4	3σ: < 58

Notes.
[a] Mean and error in mean of UV luminosity in units of $10^{11}\,L_\odot$.
[b] Infrared luminosity, in units of $10^{11}\,L_\odot$, derived from color-matching and normalizing the Dale & Helou (2002) models to the observed fluxes. For Sample F, we assume the upper limit in L_{IR} implied by the observed fluxes at 24 and 160 μm and the upper limit at 100 μm and 1.4 GHz.
[c] Dust correction factor required to recover the total SFR from the UV-determined SFR.
[d] Median star formation rates in $M_\odot$ yr^{-1} assuming a Salpeter (1955) IMF from 0.1 to 100 $M_\odot$ and the Kennicutt (1998) relations between UV/IR luminosity and star formation rate. For the "young" subsample (Sample F), we multiply the UV SFR determined from the Kennicutt (1998) relation by a factor of two. This is done to account for the fact that the mix of O and B stars contributing to the UV continuum emission has not equilibrated for ages $\lesssim$100 Myr (assuming a constant star formation); thus, the Kennicutt (1998) conversion between UV luminosity and SFR will underpredict the total SFR for such "young" galaxies.

from that computed based on the unobscured UV luminosity as $(SFR_{IR}+SFR_{UV})/SFR_{UV} \equiv 1+ SFR_{IR}/SFR_{UV}$. For the L^* sample, the median dust obscuration is $L_{IR}/L_{UV} = 7.1 \pm 1.1$, the ratio of obscured to unobscured SFR is $SFR_{IR}/SFR_{UV} = 4.2 \pm 0.6$, and the dust correction factor is 5.2 ± 0.6. The L_{UV}, L_{IR}, ratio of obscured to unobscured SFR, and total SFR for each subsample are listed in Table 5. For the conversion to SFR, we assume a Salpeter (1955) IMF with limits from 0.1 to 100 $M_\odot$ and the Kennicutt (1998) conversions between UV/IR luminosity and SFR. The results indicate that roughly 80% of the star formation is obscured for L^* galaxies at $z \sim 2$.

The dust obscuration varies between $L_{IR}/L_{UV} = 4.8 \pm 1.0$ for the subsample with blue UV slopes (Sample C) and $L_{IR}/L_{UV} = 10.7 \pm 1.9$ for the subsample with red UV slopes (Sample D), and is as high as $L_{IR}/L_{UV} \approx 37.7 \pm 7.9$ for the most bolometrically luminous galaxies (Sample E). These observations imply a trend in dustiness with both UV slope and bolometric luminosity.

5.2.2. Validity of the UV Attenuation Curve for L^* Galaxies at $z \sim 2$

We show the dust obscuration derived for these samples as a function of UV slope, β, in Figure 8. Up to luminosities of $L_{IR} \approx 10^{12}\,L_\odot$, we find that galaxies with redder β are on average dustier. Furthermore, the correlation between dustiness and UV slope is essentially identical to that found for local starburst galaxies (Meurer et al. 1999; Calzetti et al. 2000). This result has been found by several other investigations targeting moderately luminous galaxies and using a variety of star formation tracers at $z \sim 2$ (e.g., Reddy & Steidel 2004; Reddy et al. 2006b, 2010; Daddi et al. 2007; Pannella et al. 2009) and $z \sim 3$ (e.g., Seibert et al. 2002; Nandra et al. 2002; Magdis et al. 2010a, 2010b).

Infrared selection, e.g., such as 24 μm selection, generally results in samples where the bulk of galaxies do not abide by the Meurer et al. (1999) or Calzetti et al. (2000) attenuation curves (e.g., Murphy et al. 2011). As discussed in Reddy et al. (2006b, 2010), the correlation between UV slope and dust attenuation breaks down for more infrared luminous galaxies at $z \sim 2$, as well as younger galaxies with ages $\lesssim$100 Myr at the same redshifts, where the latter tend to follow a steeper attenuation curve (i.e., they are less reddened at a given UV slope than predicted by the Meurer et al. 1999 relation). Systematic deviations from the local starburst attenuation curve have also been observed at lower redshift ($z \lesssim 2$) based on *Herschel*/PACS and SPIRE data (e.g., Buat et al. 2010; Burgarella et al. 2011) and *Akari* data (Buat et al. 2011).

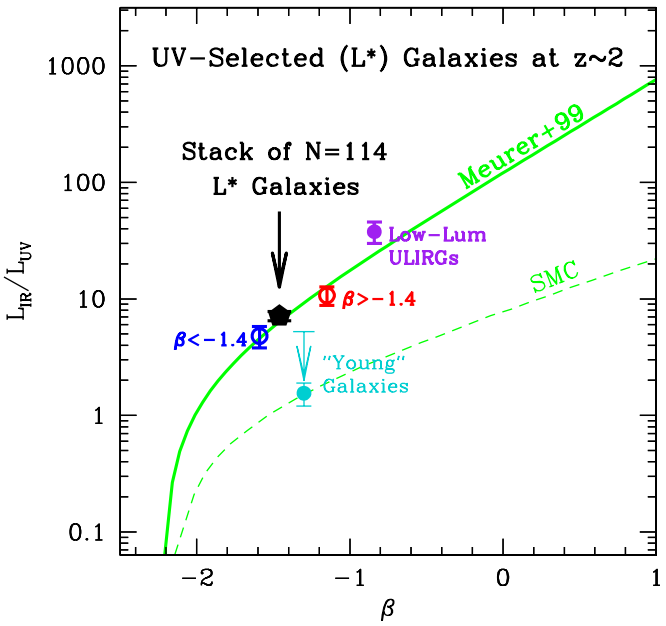

Figure 8. Mean dust attenuation (L_{IR}/L_{UV}) vs. UV slope (β) for different subsamples of $z \sim 2$ galaxies. Also shown are attenuation curves for the SMC and for local UV starbursts from Meurer et al. (1999), and the 3σ upper limit and stacked 24 μm implied value (cyan point) of the dust attenuation for the youngest galaxies in our sample. For a consistent comparison, we have shifted the original relation between dust attenuation and β from Meurer et al. (1999) upward by 0.24 dex to account for the fact that these authors defined the dust attenuation using the far-infrared luminosity, $L_{FIR} \equiv L(40\text{–}120\,\mu\text{m})$, instead of $L_{IR} \equiv L(8\text{–}1000\,\mu\text{m})$ as is done here.
(A color version of this figure is available in the online journal.)

Much of the aforementioned deviation from the local starburst attenuation curve can be understood in the context of the range of bolometric luminosity probed by the different UV and IR

selections. UV color selection is sensitive to galaxies with moderate (L^*) luminosities and lower dust extinction than those selected in the infrared. Because dust attenuation is a strong function of bolometric luminosity and the validity of the Meurer et al. (1999) relation is luminosity dependent (Meurer et al. 1999; Goldader et al. 2002; Reddy et al. 2006b, 2010), it is natural to expect departures from this relation for galaxies that may be selected via their infrared emission. Deviations may also be observed in infrared luminous galaxies that also have large stellar masses; in this case, the UV continuum associated with the massive OB stars may be extinguished relative the UV emission from less massive stars, resulting in a redder UV continuum slope for a given dust obscuration (e.g., Murphy et al. 2011; Buat et al. 2010). These results stress that one must take care in applying *any* starburst attenuation curve to high-redshift galaxies, with the realization that such relations may apply in one regime but fail in another depending on the properties of the galaxies in one's sample. Here, we have shown that galaxies that lie around L^* of the UV LF have dust obscuration—as measured from *Spitzer*, *Herschel*, and VLA data—that correlate with their UV slopes, and that this correlation is similar to that observed for local starburst galaxies.

The stacked *Herschel* data do not directly indicate the intrinsic dispersion in the relation between UV slope and dustiness. However, an indirect estimate of this scatter comes from an analysis of the 24 μm data. Specifically, 109 of 311 galaxies in the larger (and multiple field) sample of Reddy et al. (2010) are detected at 24 μm. Using a survival analysis to take into account both detections and non-detections, Reddy et al. (2010) found a dispersion of ≈0.40 dex between dust attenuation, $L_{\rm IR}/L_{\rm UV}$, and rest-UV slope, β. If the scatter in the L_8-to-$L_{\rm IR}$ ratio is similar to that found by Elbaz et al. (2011) for lower redshift ($z \lesssim 2.0$) galaxies with $L_{\rm IR} \lesssim 10^{12}\,L_\odot$ (having a 1σ dispersion of ≈0.1 dex), then the implied total dispersion in the relation between dustiness and UV slope is ≈0.45 dex. The correspondence between $L_{\rm IR}/L_{\rm UV}$ and β to within a factor of ≈3 thus verifies the applicability of the Meurer et al. (1999) and Calzetti et al. (2000) attenuation curves for galaxies with $L_{\rm IR} \lesssim 10^{12}\,L_\odot$ at $z \sim 2$. The UV attenuation curve is sensitive primarily to the geometry of dust and stars within galaxies, and/or variations in dust composition. Hence, the correspondence of the UV attenuation curves between local starbursts and $z \sim 2$ L^* galaxies implies a remarkable similarity in the processes that give rise to the spatial distribution of dust and stars and the dust composition in galaxies over ≈10 billion years of cosmic history.

5.3. Comparison with Recent Studies

Using the *Herschel* data to directly probe the thermal dust emission, we have shown that the local correlation between UV slope and dust obscuration remains valid for typical star-forming galaxies at $z \sim 2$. In the following, we compare our results with several recent studies of the dust attenuation of high-redshift galaxies.

5.3.1. Radio Emission from UV-selected Galaxies

Carilli et al. (2008) stack the radio emission of $z \sim 3$ LBGs in the COSMOS field and deduce that $\rm SFR_{radio}/SFR_{UV} = 1.8 \pm 0.4$, where $\rm SFR_{radio}$ is derived using the calibration of Yun et al. (2001). This calibration is based on equating the local SFR density with the integral of the radio LF, so in this case the radio SFR should represent a total SFR (but see below), including obscured and unobscured components. The factor of 1.8 from the Carilli et al. (2008) study is significantly smaller than the factor of ≈5 computed for our UV-selected sample at $z \sim 2$.

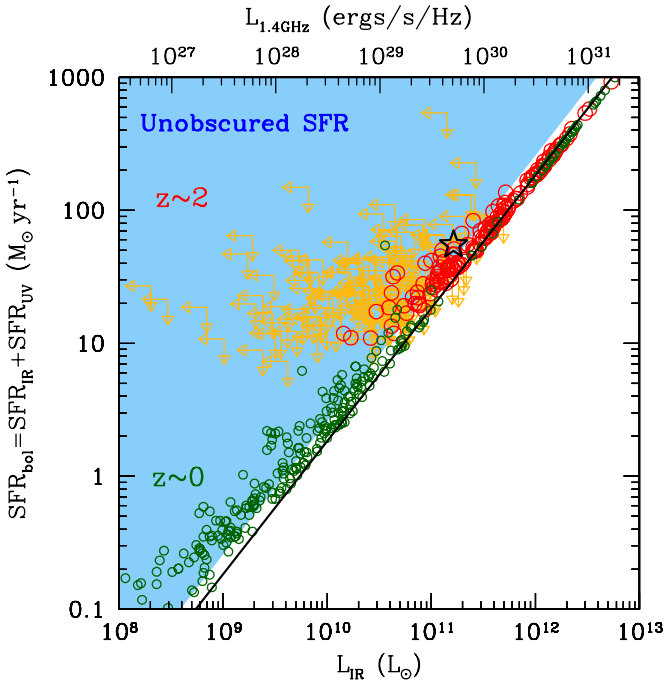

Figure 9. Total star formation rate vs. infrared luminosity ($L_{\rm IR}$) for the sample of 392 UV-selected $z \sim 2$ galaxies of Reddy et al. (2010) (red circles and orange upper limits), and the local samples of Bell (2003) and Huang et al. (2009) (dark green circles). The top axis shows the radio luminosity that corresponds to $L_{\rm IR}$ assuming the radio–IR correlation of Yun et al. (2001), and the solid line denotes the relationship between radio luminosity and star formation rate derived in that study. The shaded region covers the area where the unobscured star formation is at least 50% of the obscured star formation. The large open star denotes the position of the COSMOS LBGs from Carilli et al. (2008).

(A color version of this figure is available in the online journal.)

Carilli et al. (2008) discuss several possibilities for the suppression of radio flux with respect to SFR at $z \sim 3$. For a consistent comparison, we assess their results using the same calibration used in this analysis. In particular, we employ the Bell (2003) correlation between total infrared luminosity ($L_{\rm IR}$) and specific luminosity at 1.4 GHz. Doing so, the stacked median radio luminosity of LBGs in the COSMOS field, $L_{1.4} = 5.1 \times 10^{29}$ erg s^{-1} Hz^{-1}, corresponds to $L_{\rm IR} \approx 2.2 \times 10^{11}\,L_\odot$. These values are essentially identical to those determined for our L^* sample at $z \sim 2$: $L_{1.4} = (5.2 \pm 1.0) \times 10^{29}$ erg s^{-1} Hz^{-1} and $L_{\rm IR} = (2.2 \pm 0.3) \times 10^{11}\,L_\odot$ (Table 4). The *obscured* SFR corresponding to the $L_{\rm IR}$ for the COSMOS LBGs, assuming the Kennicutt (1998) relation, is ≈38 $M_\odot$ yr^{-1}. Hence, the factor that we compute to recover the total SFR from the UV star formation for the Carilli et al. (2008) sample, assuming their value of the unobscured SFR of 17 $M_\odot$ yr^{-1}, is $1+38/17 \approx 3.2$. This is close to a factor of two larger than the value of 1.8 given in Carilli et al. (2008). This discrepancy results from the fact that while the Yun et al. (2001) correlation between radio luminosity and SFR gives an SFR that is in good agreement with that inferred from $L_{\rm IR}$ (SFR $\simeq$ 38 $M_\odot$ yr^{-1}), it underestimates the total SFR ($\rm SFR_{IR}+SFR_{UV}$) of $\simeq$55 $M_\odot$ yr^{-1}.

To illustrate this point, we plot in Figure 9 the relationship between *total* SFR and infrared luminosity, adopting the Kennicutt (1998) conversions between UV/IR luminosity and SFR, for the sample of 392 $z \sim 2$ galaxies of Reddy et al. (2010), and for the local samples of Bell (2003) and Huang et al.

(2009). The top axis in Figure 9 indicates the radio luminosity that corresponds to L_{IR} assuming the Yun et al. (2001) calibration, and the solid line shows the relationship between radio luminosity and SFR derived in that study. The Yun et al. (2001) calibration is valid if most of the star formation is obscured, as is the case for ULIRGs at both $z \sim 2$ and $z \sim 0$. However, a substantial fraction of the LIRGs in the $z \sim 2$ sample have a significant contribution from unobscured star formation, where the unobscured component is at least 50% of the obscured star formation. The same is true for the COSMOS LBG sample of Carilli et al. (2008). The ratio of obscured to unobscured SFR is a strong function of total SFR or bolometric luminosity (e.g., Figure 9; Reddy et al. 2010), and the UV component obviously cannot be neglected for objects that have significant UV emission. Figure 9 shows that one would significantly underestimate the total SFR of LIRGs at $z \sim 2$ based on their IR emission alone (the Kennicutt 1998 relation between SFR and L_{IR} is only valid in the optically thick limit), or based on using the Yun et al. (2001) relationship between radio luminosity and SFR.

Note also that Carilli et al. (2008) combine the *median* radio SFR with the *mean* unobscured UV SFR to determine the effect of dust. In general, mean luminosities will be larger than median ones for a population drawn from a Schechter (1976) LF, modulo sample incompleteness. For our L^* sample, the mean UV luminosity is about 15% larger than the median. More importantly, the *mean* unobscured UV luminosity of the Carilli et al. (2008) sample of 17 $M_\odot$ yr^{-1} is about a factor of two larger than the *median* UV SFR for our L^* sample of $\approx$8.5 $M_\odot$ yr^{-1}. It is possible that the relatively UV-bright LBGs of the Carilli et al. (2008) sample are somewhat less attenuated than more typical (and less UV-luminous) LBGs at $z \sim 2$–3, though this is contrary to what has been found for UV-selected galaxies at these redshifts (Reddy et al. 2010). Without further analysis of their candidates, we conclude that the lower UV obscuration factor deduced by Carilli et al. (2008) is likely due to the brighter unobscured UV luminosity of their candidates, relative to the obscured star formation. What is clear from our spectroscopic sample is that the stacked radio flux for UV-selected galaxies at $z \sim 2$ predicts an L_{IR} that is identical to that obtained using direct measurements of thermal dust emission from the *Herschel* data, and this value of L_{IR} implies a dust correction of a factor of $\approx$5.

5.3.2. Investigations of the Extragalactic Background Light (EBL)

A second and more recent study that has suggested obscuration factors that are different from those predicted from the Meurer et al. (1999) relation comes from an analysis of the infrared background based on stacked *Spitzer* and Balloon-borne Large-Aperture Submillimeter Telescope data by Chary & Pope (2010). These authors estimate the extragalactic background light (EBL) contributed from galaxies at $z \gtrsim 1$ and conclude that the UV-based dust corrections for typical star-forming galaxies (e.g., those selected by their UV emission) must be lower than the Meurer et al. (1999) prediction in order that their integrated emission does not violate the background light constraints. However, directly probing the thermal dust emission of L^* galaxies at $z \sim 2$, as we have done here, shows conclusively that these galaxies have dust attenuations that are similar, on average, to those computed based on the Meurer et al. (1999) and Calzetti et al. (2000) attenuation curves (Figure 8). How can we reconcile these two results?

The EBL is sensitive to the average dust attenuation of *all* galaxies, not just the UV-bright ones studied here. Indeed, Reddy & Steidel (2009) and Reddy et al. (2010) use physical arguments and stacked *Spitzer* data to show that the dust obscuration of UV-faint galaxies is lower than in UV-bright ones (see also the next section) and that this luminosity dependence implies that the average dust obscuration, integrated over the entire LF, can be close to a factor of two lower than the mean dust obscuration found for just the UV-bright galaxies (see Table 5 of Reddy & Steidel 2009). This does not necessarily imply a failure of the Meurer et al. (1999) relation for typical star-forming galaxies at high redshift; it simply means that the rest-frame UV slope also becomes bluer, on average, for UV-faint galaxies, as the empirical evidence seems to indicate at $z \sim 2.5$ (Bouwens et al. 2009). What is clear from the present analysis is that the direct measurements of the thermal dust emission of UV-selected galaxies at $z \sim 2$ imply that the local UV attenuation curve remains valid for these galaxies.

5.3.3. Stacked Herschel/SPIRE Measurements for $z \sim 2$ UV-selected Galaxies

Strong source confusion in the *Herschel*/SPIRE 250, 350, and 500 μm data makes it very difficult to carry out stacking experiments capable of reaching flux limits as faint as those we expect for L^* UV-selected galaxies at $z \sim 2$ (approximately 1 mJy—see Figure 6). After some experimentation, we have chosen not to include those data in our analysis. Nevertheless, Rigopoulou et al. (2010) stack SPIRE 250 μm data for a smaller sample of brighter, 24 μm-detected, UV-selected galaxies at $z \sim 2$. These were taken from the sample of Reddy et al. (2006a), also used here, but were limited to 69 objects with individual 24 μm detections. That subsample is therefore likely to be more IR luminous, on average, than the larger sample considered here, where individual detection at 24 μm is not required. Rigopoulou et al. (2010) measure a stacked 250 μm flux of $f_{250} = 2.7 \pm 0.8$ mJy, corresponding to a total infrared luminosity $L_{IR} \approx 4.2 \times 10^{11}\ L_\odot$ at $\langle z \rangle \approx 2$.[23] This value is similar to what we predict at 250 μm when we stack the 100 and 160 μm data for the same set of galaxies (i.e., the brighter objects with individual 24 μm detections). Given that we have (1) controlled for issues of clustering and confusion at 100 μm, and cross-checked the 160 μm fluxes with those obtained at 100 μm and (2) performed detailed simulations to demonstrate the robustness of the stacked fluxes (Section 3), we believe the PACS constraints on the median IR SED to be robust. With the PACS data we are able to constrain the median IR SED for L^* galaxies with lower average infrared luminosities, irrespective of whether they are individually detected at 24 μm. Future observations with the Atacama Large Millimeter Array (ALMA) should provide higher resolution and more sensitive observations of the Rayleigh–Jeans emission from typical star-forming galaxies at high redshift.

5.4. Dependence of Dust Attenuation on Stellar Population Age and Luminosity

5.4.1. Galaxies with "Young" ($\lesssim$100 Myr) Stellar Population Ages

Roughly 14% of the galaxies in our entire sample are identified as having a "young" stellar population with inferred

[23] We note that the stacked 250 μm flux shown in Figure 2 of Rigopoulou et al. (2010) appears to be nearly 10× fainter than the value quoted in the text. The authors state that they derive a total infrared luminosity $L_{IR} = (1.5 \pm 0.5) \times 10^{11}\ L_\odot$ using the CE01 dust templates, but we are unable to reproduce this, finding instead a luminosity that is 2.8× larger, based on the value $f_{250} = 2.7$ mJy quoted in the text.

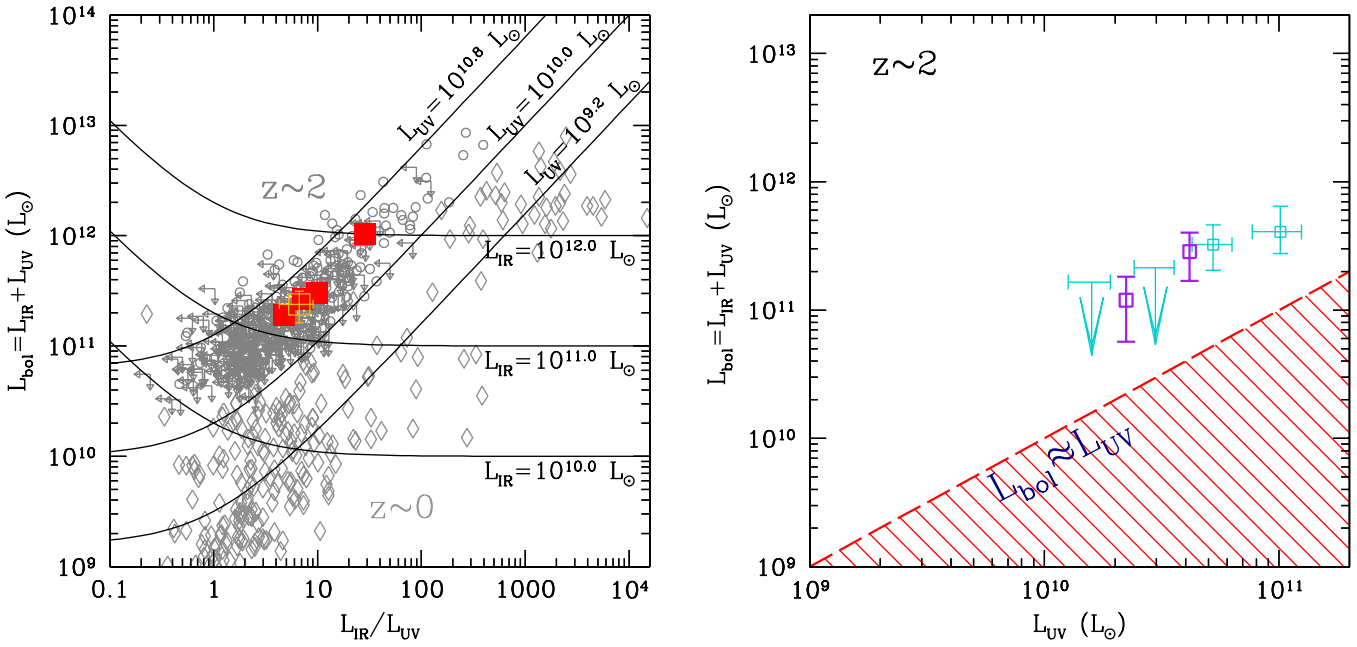

Figure 10. Left: bolometric luminosity, $L_{\rm bol} \equiv L_{\rm IR} + L_{\rm UV}$, as a function of $L_{\rm IR}/L_{\rm UV}$ for a sample of local galaxies from Bell (2003) and Huang et al. (2009), shown by the open diamonds. The sample of 392 UV-selected galaxies at $1.5 \leqslant z < 2.6$ analyzed in Reddy et al. (2010) are shown by the open circles and upper limits. The relationship between $L_{\rm bol}$ and $L_{\rm IR}/L_{\rm UV}$ for Samples A, C, D, and E, based on the stacked *Herschel*, *Spitzer*, and VLA data, is denoted by the large filled squares (error bars are not shown for clarity). The same quantity for the L^* sample at $z \sim 2$ (Sample B) is shown by the large open square. Right: correlation between $L_{\rm bol}$ and $L_{\rm UV}$, where the cyan points denote the results using 24 μm data and the Reddy et al. (2010) calibration between L_8 and $L_{\rm IR}$. The purple points indicate results from incorporating the *Spitzer*/MIPS 24 μm, *Herschel*/PACS 100 and 160 μm, and VLA 1.4 GHz data to determine the median IR SED as a function of UV luminosity.
(A color version of this figure is available in the online journal.)

ages of $\lesssim$100 Myr. Stacking these galaxies results in a formal non-detection (S/N $\lesssim$ 3) in the *Herschel* and VLA stacks (Table 2). The implied 3σ upper limit to the dust obscuration suggests that these galaxies follow an attenuation curve that is "steeper" than the typically assumed Meurer et al. (1999) and Calzetti et al. (2000) attenuation curves (Figure 8), in the sense that they exhibit a redder UV slope for a given obscuration. More stringent constraints on the dust attenuation of these galaxies come from their stacked 24 μm emission. Assuming the DH02 template that best matches the median 24 μm flux of the "young" galaxies implies $L_{\rm IR}/L_{\rm UV} \approx 1.55 \pm 0.35$. The median UV slope of these galaxies of $\beta = -1.30$ then implies that their dust obscurations are consistent with the Small Magellanic Cloud (SMC) attenuation curve. The deviation of such young, high-redshift galaxies from the standard attenuation curve is a result first noted in Reddy et al. (2006b) and further investigated in Reddy et al. (2010). IRS spectroscopy of a couple of young lensed LBGs provides additional evidence that such young galaxies are less dusty at a given UV slope (Siana et al. 2008, 2009) than their older and more typical counterparts at the same redshifts (Reddy et al. 2010).

The small carbonaceous dust grains giving rise to the mid-IR emission are believed to be produced in asymptotic giant branch stars over a longer timescale than the Type II supernovae (SNe) responsible for the large grains that emit thermally in the infrared (e.g., Galliano et al. 2008). It is therefore relevant to ask whether evolution in the small-to-large dust grain ratio may be responsible for the observed differences in attenuation curve with stellar population age. Based on an X-ray stacking analysis and an examination of the theoretical polycyclic aromatic hydrocarbon (PAH) metallicity from dust models, Reddy et al. (2010) argued that the small-to-large dust grain ratio is unlikely to change significantly over the relatively narrow range in metallicity probed by the UV-selected sample. IRS spectroscopy of at least a couple of young lensed LBGs at high-redshift also indicates that their ratios of mid-to-far IR emission are similar to those found for local starburst galaxies (Siana et al. 2008, 2009) and similar to the ratios observed for $z \sim 2$ galaxies (Reddy et al. 2006b, 2010). The *Herschel* observations, which probe the thermal dust emission at $z \sim 2$, are consistent with these findings based on 24 μm emission alone.

If the difference in attenuation curve is due purely to geometrical effects, then it suggests that the dust covering fraction of high-redshift galaxies evolves significantly with time. A possible simple scenario is one in which the first generation of stars quickly pollutes the interstellar medium (ISM) with dust and metals over a dynamical timescale of a few tens of millions of years, at which point much of the dust is foreground to the stars and the dust covering fraction is high. As star formation proceeds and either becomes spatially extended or is able to drive outflows sufficient in momentum to perturb the dust/gas distribution of the ISM, the resulting attenuation becomes patchier. So, we might expect in this situation that galaxies would gradually transition from a steep attenuation curve like that of the SMC to a grayer starburst attenuation curve (e.g., Meurer et al. 1999; Calzetti et al. 2000; see also discussion in Buat et al. 2011). Detailed studies of the variation of the interstellar absorption lines (as a proxy for the dust covering fraction) with dust attenuation will be needed to test this scenario.

5.4.2. Variation in Dust Attenuation with Bolometric and UV Luminosity

MIPS 24 μm studies have shown that $z \sim 2$ galaxies follow a tight trend between bolometric luminosity and dust attenuation (e.g., Reddy et al. 2010, and references therein), similar to that observed locally and at $z \sim 1$ (Burgarella et al. 2009; Buat et al. 2007, 2009; Wang & Heckman 1996). However,

the normalization of this trend depends on redshift, such that at a given bolometric luminosity, galaxies at high redshift are on average less dusty than local ones (Reddy et al. 2006b, 2008, 2010). This result is not unique to our UV-selected sample. Rest-frame optical, near-IR, and submillimeter selected galaxies at $z \sim 2$ also show a similar offset in obscuration per unit star formation compared with local galaxies (Reddy et al. 2006b). Reddy et al. (2010) demonstrate that this relationship is likely driven by metallicity evolution. The stacked *Herschel* and radio data confirm these previous results (Figure 10). This is not surprising given the similarity in $L_{\rm IR}$ and dust attenuation inferred in this study with those inferred for L^* galaxies based on 24 μm data alone. The combined *Herschel*, *Spitzer*, and VLA data confirm that $L^*_{\rm UV}$ galaxies at $z \sim 2$ are a factor of $\approx$10 less dusty than galaxies with similar bolometric luminosities in the local universe. Similarly, $L^*_{\rm UV}$ galaxies at $z \sim 2$ are a factor of $\approx$20–30 times more bolometrically luminous than local galaxies with a similar dust obscuration (Figure 10). These evolutionary effects can also be seen in Figure 9. In the local universe, it is only for galaxies with $L_{\rm IR} \lesssim 10^{11}\,L_\odot$ (i.e., galaxies fainter than LIRGs) where the unobscured star formation begins to contribute significantly to the total SFR. In contrast, most lower luminosity LIRGs at $z \sim 2$ have a significant fraction of unobscured star formation, as indicated by the plume of $z \sim 2$ galaxies extending away from the $\rm SFR_{bol} = SFR_{IR}$ line in Figure 9, indicating that LIRGs at $z \sim 2$ are more UV-transparent relative to LIRGs in the local universe.

Finally, we note that Reddy et al. (2010) use a 24 μm analysis of a larger sample of UV-selected galaxies at $z \sim 2$ to show that the fraction of 24 μm detections of these galaxies decreases by a factor of two proceeding from UV-bright ($L_{\rm UV} \approx 10^{11}\,L_\odot$) to UV-faint ($L_{\rm UV} \approx 10^{10}\,L_\odot$) galaxies (see Figure 14 in Reddy et al. 2010). This UV luminosity trend in 24 μm detection fraction implies that UV-faint galaxies are on average less infrared-luminous than their UV-bright counterparts, a result that is further confirmed by stacking the 24 μm emission of galaxies in bins of UV luminosity. A stacking of the combined *Spitzer*, *Herschel*, and VLA data as a function of UV luminosity shows a similar trend, indicating that UV-faint galaxies are also less bolometrically luminous than UV-bright galaxies (Figure 10). The actual dust attenuation, $L_{\rm IR}/L_{\rm UV}$, is roughly constant (within the uncertainties) with decreasing UV luminosity, as both UV and IR luminosities decrease in tandem. In any case, it is clear from these observations that care must be taken when inferring the average dust obscuration and $L_{\rm IR}$, and their effect on global quantities like the SFR density, given the UV luminosity dependence of these quantities (Reddy et al. 2008; Reddy & Steidel 2009).

6. CONCLUSIONS

We have used the deep 100 and 160 μm data of the GOODS-*Herschel* Open Time Key Program, supplemented with deep *Spitzer*/MIPS 24 μm and VLA 1.4 GHz radio imaging, to investigate the infrared luminosities and dust obscuration of typical star-forming galaxies at high redshift. We focus on the median stacked mid-infrared, far-infrared, and radio fluxes of a sample of 146 UV-selected galaxies with spectroscopic redshifts $1.5 \leqslant z_{\rm spec} < 2.6$ in the GOODS-North field. These galaxies have luminosities around L^* of the UV LF at these redshifts.

Because these galaxies are individually undetected at 100, 160 μm, and 1.4 GHz, we perform median stacking analyses to measure their average fluxes. Three tests are performed to verify the robustness of our stacked results. The first test measured the effects of clustering. The second test determined the chance probability of measuring a stacked flux as high as the one obtained for the target galaxies. The third test allows us to measure the biases and uncertainties in stacked flux measurements by stacking on the positions of artificial sources added to the images.

To interpret these fluxes, we consider a variety of dust templates, including those of Elbaz et al. (2011), Chary & Elbaz (2001), Dale & Helou (2002), and Rieke et al. (2009), as well as the 24 μm–$L_{\rm IR}$ and radio–IR correlations of Reddy et al. (2010) and Bell (2003), respectively. Fitting these templates to the bias-corrected fluxes and infrared colors reveals that $L^*_{\rm UV}$ galaxies at $z \sim 2$ with UV luminosities $L_{\rm UV} \gtrsim 10^{10}\,L_\odot$ have a median infrared luminosity of $L_{\rm IR} = (2.2 \pm 0.3) \times 10^{11}\,L_\odot$. Galaxies in our sample exhibit $L_{\rm IR}/L_8$ (IR8) ratios that are a factor of $\approx$2 larger than those found for most star-forming galaxies at lower redshifts, likely due to the fact these UV-selected galaxies are relatively compact for their infrared luminosity. One possibility is that the roughly constant IR8 ratio observed for most (main-sequence) galaxies with redshifts $z \lesssim 2.0$ likely shifts toward larger values at $z \gtrsim 2.0$, due to the fact that the galaxies are on average smaller for their IR luminosity relative to lower redshift galaxies.

Stacking the *Spitzer*, *Herschel*, and VLA data as a function of UV spectral slope, β, and bolometric luminosity, $L_{\rm bol}$, indicates that galaxies with redder β and higher $L_{\rm bol}$ have on average larger infrared luminosities, in accord with expectations based on trends found for local star-forming galaxies. Based on the $L_{\rm IR}$, we proceed to examine the dust attenuation, $L_{\rm IR}/L_{\rm UV}$, and the dust correction factor (i.e., the factor required to recover the bolometric SFR from the unobscured UV SFR), $1+\rm SFR_{IR}/SFR_{UV}$, for galaxies in our sample. For L^* galaxies at $z \sim 2$, we find a dust attenuation of $L_{\rm IR}/L_{\rm UV} = 7.1 \pm 1.1$, which corresponds to a dust correction factor of 5.2 ± 0.6, implying that $\simeq$80% of the star formation is obscured. This result is consistent with those found in previous studies of the dust-corrected UV and Hα, 24 μm, and radio and X-ray stacks of the same galaxies examined here (Reddy & Steidel 2004; Reddy et al. 2006b, 2010).

We have examined the relationship between the UV spectral slope, β, and dustiness for $z \sim 2$ galaxies. A small fraction ($\approx$14%) of galaxies are identified as having stellar population ages $\lesssim$100 Myr from fitting stellar population SEDs to the observed optical through near-IR photometry. The upper limit in dust attenuation for these "young" galaxies suggests that they may follow a "steeper" attenuation curve than the one observed for local starburst galaxies (Meurer et al. 1999; Calzetti et al. 2000), in the sense that they are less dusty (i.e., have lower $L_{\rm IR}/L_{\rm UV}$ ratios) for a given β than older and more typical galaxies at the same redshift. This result was first noted in the 24 μm analyses of Reddy et al. (2006b) and further investigated in Reddy et al. (2010), and may be attributable to the higher dust covering fractions in young galaxies. When considering more typical galaxies with ages $\gtrsim$ 100 Myr, we find that their median $L_{\rm IR}/L_{\rm UV}$ increases as β becomes redder and that this correlation is essentially identical to that found for local starbursts (Meurer et al. 1999; Calzetti et al. 2000). Comparison of the *Herschel* results at $z \sim 2$ with measurements of local galaxies confirms the previously found trends that imply that LIRGs at $z \sim 2$ are more UV transparent (i.e., less dusty) than LIRGs in the local universe, and that UV-faint galaxies at $z \sim 2$ have lower $L_{\rm IR}$ and hence fainter bolometric luminosities than UV-bright galaxies at $z \sim 2$ (e.g., see also Reddy et al. 2010). Based on the

direct *Herschel* measurements of the rest-frame $\simeq$30 and 50 μm thermal dust emission, we find that the local UV attenuation curve holds at $z \sim 2$ for galaxies with $L_{\rm bol} \lesssim 10^{12}\,L_{\odot}$, suggesting a remarkable similarity in the processes governing star formation and dust production over the last 10 billion years of cosmic time.

We have made significant progress in evaluating the effects of dust in typical star-forming galaxies at $z \sim 2$ as traced by thermal infrared emission. However, even the superb sensitivity and resolution of *Herschel* are not sufficient to individually detect L^* galaxies at these redshifts. The most accurate estimate of dust luminosity, and hence total SFR, can only come from combining *individual* measurements of UV and IR luminosities. Though the observations will be targeted, ALMA promises to extend our knowledge of the dust continuum luminosities of *individual* star-forming galaxies at $z \sim 2$, thus providing the key ingredient to combine with UV measurements. These developments point to a wealth of forthcoming information on the properties of dust in typical star-forming galaxies at high redshift. Ultimately, a robust characterization of the relationship between infrared and short wavelength (UV, Hα) emission will be crucial for inferring dust attenuation and total SFRs of the very faint and/or very high redshift galaxies that will be inaccessible to even the next generation of long wavelength observatories.

Support for N.A.R. was provided by NASA through Hubble Fellowship grant HST-HF-01223.01 awarded by the Space Telescope Science Institute, which is operated by the Association of Universities for Research in Astronomy, Inc., for NASA, under contract NAS 5-26555. This work is based on observations made with the *Herschel Space Observatory*, a European Space Agency Cornerstone Mission with significant participation by NASA. Support for this work was provided by NASA through an award issued by JPL/Caltech.

REFERENCES

Adelberger, K. L., & Steidel, C. C. 2000, ApJ, 544, 218
Adelberger, K. L., Steidel, C. C., Shapley, A. E., et al. 2004, ApJ, 607, 226
Alexander, D. M., Bauer, F. E., Brandt, W. N., et al. 2003, AJ, 126, 539
Appleton, P. N., Fadda, D. T., Marleau, F. R., et al. 2004, ApJS, 154, 147
Bell, E. F. 2003, ApJ, 586, 794
Bourne, N., Dunne, L., Ivison, R. J., et al. 2011, MNRAS, 410, 1155
Bouwens, R. J., Illingworth, G. D., Franx, M., et al. 2009, ApJ, 705, 936
Buat, V., Giovannoli, E., Burgarella, D., et al. 2010, MNRAS, 409, L1
Buat, V., Giovannoli, E., Takeuchi, T. T., et al. 2011, A&A, 529, A22
Buat, V., Iglesias-Páramo, J., Seibert, M., et al. 2005, ApJ, 619, L51
Buat, V., Marcillac, D., Burgarella, D., et al. 2007, A&A, 469, 19
Buat, V., Takeuchi, T. T., Burgarella, D., Giovannoli, E., & Murata, K. L. 2009, A&A, 507, 693
Burgarella, D., Buat, V., Takeuchi, T. T., Wada, T., & Pearson, C. 2009, PASJ, 61, 177
Burgarella, D., Heinis, S., Magdis, G., et al. 2011, ApJ, 734, L12
Calzetti, D. 1997, AJ, 113, 162
Calzetti, D., Armus, L., Bohlin, R. C., et al. 2000, ApJ, 533, 682
Carilli, C. L., Lee, N., Capak, P., et al. 2008, ApJ, 689, 883
Chary, R., & Elbaz, D. 2001, ApJ, 556, 562
Chary, R., & Pope, A. 2010, arXiv:1003.1731
Condon, J. J. 1992, ARA&A, 30, 575
Daddi, E., Dickinson, M., Morrison, G., et al. 2007, ApJ, 670, 156
Dale, D. A., & Helou, G. 2002, ApJ, 576, 159
Dickinson, M., Giavalisco, M., & The Goods Team 2003, in The Mass of Galaxies at Low and High Redshift, ed. R. Bender & A. Renzini (Berlin: Springer), 324
Elbaz, D., Dickinson, M., Hwang, H. S., et al. 2011, A&A, 533, 119
Elbaz, D., Hwang, H. S., Magnelli, B., et al. 2010, A&A, 518, L29
Engelbracht, C. W., Gordon, K. D., Rieke, G. H., et al. 2005, ApJ, 628, L29
Erb, D. K., Steidel, C. C., Shapley, A. E., et al. 2006, ApJ, 647, 128
Förster Schreiber, N. M., van Dokkum, P. G., Franx, M., et al. 2004, ApJ, 616, 40
Galliano, F., Dwek, E., & Chanial, P. 2008, ApJ, 672, 214
Giavalisco, M., Ferguson, H. C., Koekemoer, A. M., et al. 2004, ApJ, 600, L93
Goldader, J. D., Meurer, G., Heckman, T. M., et al. 2002, ApJ, 568, 651
Heckman, T. M., Robert, C., Leitherer, C., Garnett, D. R., & van der Rydt, F. 1998, ApJ, 503, 646
Helou, G., Malhotra, S., Hollenbach, D. J., Dale, D. A., & Contursi, A. 2001, ApJ, 548, L73
Hogg, D. W., Tremonti, C. A., Blanton, M. R., et al. 2005, ApJ, 624, 162
Huang, J.-S., Faber, S. M., Daddi, E., et al. 2009, ApJ, 700, 183
Ivison, R. J., Magnelli, B., Ibar, E., et al. 2010, A&A, 518, L31
Kennicutt, R. C. 1998, ARA&A, 36, 189
Kennicutt, R. C., Hao, C., Calzetti, D., et al. 2009, ApJ, 703, 1672
Kong, X., Charlot, S., Brinchmann, J., & Fall, S. M. 2004, MNRAS, 349, 769
Law, D. R., Steidel, C. C., Erb, D. K., et al. 2007, ApJ, 656, 1
Madau, P. 1995, ApJ, 441, 18
Magdis, G. E., Elbaz, D., Daddi, E., et al. 2010a, ApJ, 714, 1740
Magdis, G. E., Elbaz, D., Hwang, H. S., et al. 2010b, ApJ, 720, L185
Magnelli, B., Elbaz, D., Chary, R. R., et al. 2011, A&A, 528, A35
Mao, M. Y., Huynh, M. T., Norris, R. P., et al. 2011, ApJ, 731, 79
Marcillac, D., Elbaz, D., Chary, R. R., et al. 2006, A&A, 451, 57
Meurer, G. R., Heckman, T. M., & Calzetti, D. 1999, ApJ, 521, 64
Morrison, G. E., Owen, F. N., Dickinson, M., Ivison, R. J., & Ibar, E. 2010, ApJS, 188, 178
Murphy, E. J., Chary, R.-R., Dickinson, M., et al. 2011, ApJ, 732, 126
Nandra, K., Mushotzky, R. F., Arnaud, K., et al. 2002, ApJ, 576, 625
Nordon, R., Lutz, D., Shao, L., et al. 2010, A&A, 518, L24
Normand, P., Rouan, D., Lacombe, F., & Tiphene, D. 1995, A&A, 297, 311
Oesch, P. A., Bouwens, R. J., Carollo, C. M., et al. 2010, ApJ, 709, L21
Pannella, M., Carilli, C. L., Daddi, E., et al. 2009, ApJ, 698, L116
Papovich, C., Rudnick, G., Le Floc'h, E., et al. 2007, ApJ, 668, 45
Papovich, C., Rudnick, G., Rigby, J. R., et al. 2009, ApJ, 704, 1506
Pilbratt, G. L., Riedinger, J. R., Passvogel, T., et al. 2010, A&A, 518, L1
Poglitsch, A., Waelkens, C., Geis, N., et al. 2010, A&A, 518, L2
Puget, J. L., & Leger, A. 1989, ARA&A, 27, 161
Reddy, N. A., Erb, D. K., Pettini, M., Steidel, C. C., & Shapley, A. E. 2010, ApJ, 712, 1070
Reddy, N. A., Erb, D. K., Steidel, C. C., et al. 2005, ApJ, 633, 748
Reddy, N. A., & Steidel, C. C. 2004, ApJ, 603, L13
Reddy, N. A., & Steidel, C. C. 2009, ApJ, 692, 778
Reddy, N. A., Steidel, C. C., Erb, D. K., Shapley, A. E., & Pettini, M. 2006a, ApJ, 653, 1004
Reddy, N. A., Steidel, C. C., Fadda, D., et al. 2006b, ApJ, 644, 792
Reddy, N. A., Steidel, C. C., Pettini, M., et al. 2008, ApJS, 175, 48
Richards, E. A. 2000, ApJ, 533, 611
Rieke, G. H., Alonso-Herrero, A., Weiner, B. J., et al. 2009, ApJ, 692, 556
Rigopoulou, D., Magdis, G., Ivison, R. J., et al. 2010, MNRAS, 409, L7
Roussel, H., Sauvage, M., Vigroux, L., & Bosma, A. 2001, A&A, 372, 427
Salpeter, E. E. 1955, ApJ, 121, 161
Sargent, M. T., Schinnerer, E., Murphy, E., et al. 2010, ApJ, 714, L190
Schechter, P. 1976, ApJ, 203, 297
Seibert, M., Heckman, T. M., & Meurer, G. R. 2002, AJ, 124, 46
Siana, B., Smail, I., Swinbank, A. M., et al. 2009, ApJ, 698, 1273
Siana, B., Teplitz, H. I., Chary, R.-R., Colbert, J., & Frayer, D. T. 2008, ApJ, 689, 59
Steidel, C. C., Adelberger, K. L., Shapley, A. E., et al. 2003, ApJ, 592, 728
Steidel, C. C., Pettini, M., & Hamilton, D. 1995, AJ, 110, 2519
Steidel, C. C., Shapley, A. E., Pettini, M., et al. 2004, ApJ, 604, 534
Tielens, A. G. G. M., Hony, S., van Kerckhoven, C., & Peeters, E. 1999, in The Universe as Seen by ISO, ed. P. Cox & M. F. Kessler (ESA-SP 427; Noordwijk: ESA), 579
Wang, B., & Heckman, T. M. 1996, ApJ, 457, 645
Yun, M. S., Reddy, N. A., & Condon, J. J. 2001, ApJ, 554, 803